

OPTIMIZATION OF THE ABSORBER/BUFFER INTERFACE REGION OF  $\text{Cu(In,Ga)Se}_2$   
PHOTOVOLTAIC DEVICES: A NUMERICAL SIMULATION STUDY

Yasas Patikirige

A Thesis

Submitted to the Graduate College of Bowling Green  
State University in partial fulfillment of  
the requirements for the degree of

MASTER OF SCIENCE

August 2019

Committee:

Marco Nardone, Advisor

Lewis P. Fulcher

Haowen Xi

Copyright ©August 2019

Yasas Patikirige

All rights reserved

## ABSTRACT

Dr. Marco Nardone, Advisor

Solar cells based on the compound Copper Indium Gallium Diselenide,  $\text{Cu}(\text{In}_x\text{Ga}_{1-x})\text{Se}_2$ , (or CIGS) are commercially important. The electronic properties of CIGS can be controlled by varying the composition. This thesis presents the numerical simulation to optimize the absorber (CIGS)/buffer (CdS) interface region of  $\text{Cu}(\text{In,Ga})\text{Se}_2$  thin-film photovoltaic devices. Experimental data and theory indicate that a Cu-poor CIGS region exists near the interface between the CIGS and CdS. It has been implied that the Cu-poor region forms an ordered vacancy compound (OVC) that has significant effects on device performance. In this work, we start with a benchmark device simulation compared to data, then add the OVC layer with variable properties, including the thickness, band gap, electron affinity, doping, and defect concentrations to study the effects on overall device performance. Since the band gap of CIGS can be spatially graded, we also consider the effects of common single and double graded structures. Simulations were carried out using one-dimensional simulation program SCAPS-1D and results reached maximum efficiencies of 20.1% – 20.3% for double graded composition and 22.0% – 22.2% for single graded composition. The electronic properties of the Cu-poor region do not appear to directly improve the device efficiency, yet secondary benefits should be noted, such as reducing surface defects at the CIGS/CdS heterojunction and shunting that may occur with Cu-rich deposition.

*I dedicate this thesis to my family for their affection, love and dedication  
for success in my life.*

## ACKNOWLEDGMENTS

I would like to express my sincere gratitude my advisor, Dr. Marco Nardone for all his support and valuable guidance for carrying out this research work as well as successfully finishing this thesis. I must also acknowledge the financial support from the National Renewable Energy Laboratory (NREL) and U.S Department of Energy.

Besides my advisor, I would like to thank the rest of my thesis committee: Dr. Lewis P. Fulcher and Dr. Haowen Xi for their time in reviewing this thesis.

I cannot forget my parents who made what I am today possible. Without their support, I would never have been able to succeed as I did. Thank you very much, “Amma” and “Thaththa” and my sister, Ayo for your support and encouragement.

## TABLE OF CONTENTS

	Page
CHAPTER 1 INTRODUCTION AND OBJECTIVES . . . . .	1
1.1 Background and History . . . . .	2
1.2 Generations of Photovoltaic Devices . . . . .	2
1.3 CIGS Devices . . . . .	4
1.4 Ordered Vacancy Compound Layer . . . . .	7
CHAPTER 2 THEORY . . . . .	9
2.1 Semiconductor Equations . . . . .	9
2.1.1 Drift Current . . . . .	10
2.1.2 Diffusion Current . . . . .	11
2.1.3 Generation of Electron-Hole Pairs . . . . .	12
2.1.4 Recombination . . . . .	13
2.2 Junction Formation . . . . .	14
2.3 Interface States . . . . .	16
CHAPTER 3 METHODOLOGY . . . . .	18
3.1 Numerical Calculations . . . . .	18
3.2 Baseline Models . . . . .	19
3.3 Band-gap Grading . . . . .	20
3.4 Model A with OVC Layer . . . . .	21
3.5 J-V Characteristic Curve . . . . .	22
3.6 EQE Curves . . . . .	22
CHAPTER 4 RESULTS . . . . .	25
4.1 Results for Baseline Models . . . . .	25
4.1.1 JV Curves . . . . .	25
4.1.2 EQE Curves . . . . .	25

	vii
4.2 Effects of OVC Doping, Deep Defect Density, and Thickness . . . . .	27
4.3 Effect of Band Off-Set . . . . .	30
4.4 Optimization of The Band-gap and Electron Affinity . . . . .	37
4.5 Band-gap and Defect Density . . . . .	37
4.6 Effects of Interface States on EQE . . . . .	38
CHAPTER 5 CONCLUSION . . . . .	43
BIBLIOGRAPHY . . . . .	45

## LIST OF FIGURES

Figure	Page
1.1 Basic structure of the CIGS PV device. . . . .	5
1.2 Lattice structure of CIGS. . . . .	6
1.3 Monolithic interconnect structure of CIGS modules. . . . .	7
2.1 Formation of a pn junction. . . . .	15
2.2 A figure of a simple heterojunction showing the conduction and valence band offsets.	16
3.1 Graded band gap (center panel) and electron affinity (bottom panel) based on measured Gallium profiles. . . . .	21
3.2 I-V curve for a typical solar cell in dark and light. . . . .	23
3.3 Reflectivity profile introduced for front contact. . . . .	24
4.1 JV curves for all our models and reference models with double graded composition.	26
4.2 QE curves for all our models and reference models. . . . .	28
4.3 Efficiency dependence on mid-gap donor density and shallow acceptor density in the OVC layer for double graded Ga profile. . . . .	31
4.4 Efficiency dependence on mid-gap donor density and shallow acceptor density in the OVC layer for single graded Ga profile. . . . .	32
4.5 Efficiency dependence on OVC thickness and acceptor density for double-graded and single-graded Ga composition. . . . .	33
4.6 Efficiency dependence on acceptor density at various OVC thicknesses for double-graded and single-graded Ga composition. . . . .	34
4.7 a) Open circuit voltage ( $V_{oc}$ ) b) Short circuit current density ( $J_{sc}$ ) c) Fill factor ( $FF$ ) dependence on OVC thickness and acceptor density for single graded Ga composition. . . . .	35
4.8 Band diagrams at equilibrium (0 V bias voltage) for Model A. . . . .	36

4.9	Efficiency dependence on OVC band-gap and electron affinity for a) Double graded b) Single graded Ga composition profile for 10nm thick OVC layer. . . . .	39
4.10	a) Open circuit voltage ( $V_{oc}$ ) b) Short circuit current ( $J_{sc}$ ) c) Fill factor ( $FF$ ) dependence on OVC band-gap and electron affinity for single graded Ga concentration for 10nm thick OVC layer. . . . .	40
4.11	Efficiency dependence on OVC band-gap and midgap donor type defects for double graded and single graded Ga composition profile for 100nm thick OVC layer. . . .	41
4.12	External quantum efficiency calculations . . . . .	42

## LIST OF TABLES

Table	Page
3.1 Baseline model parameters. . . . .	20
3.2 Variable parameters in OVC layer and CIGS composition. . . . .	22
4.1 Performance metrics of reference models and our calculations for models A-D with double graded composition. . . . .	26
4.2 Performance metrics of reference models and our calculations for models A-D with single graded composition. . . . .	27
5.1 Performance metrics of Model A with and without OVC layer . . . . .	43

## CHAPTER 1 INTRODUCTION AND OBJECTIVES

World energy demand is increasing each year and for centuries fossil fuels have been the primary energy source for the human race. Replacing the dominant role of fossil fuels with alternative energy sources has become one of the major concerns around the world. Among alternative energy sources, including hydroelectricity, wind power, biofuels, geothermal, and nuclear energy, solar energy is a critical renewable source of energy due to its availability and low impact to the environment [1].

Generating electricity using solar energy is achieved by photovoltaic (PV) devices. Among several types of PV device technologies at present, those based on the compound Copper Indium Gallium Diselenide,  $\text{Cu}(\text{In}_x\text{Ga}_{1-x})\text{Se}_2$ , (or CIGS) are commercially important due to several key properties, including: low cost per Watt value, thin film nature, ability of tuning the band gap of the absorber layer, and relatively inexpensive manufacturing techniques [2–4]. The electronic properties of CIGS can be controlled by varying the composition. Alkali elements, such as Na, K, Rb and Cs are typically used as dopants and passivating agents to optimize the transport properties of CIGS in a device structure [5–8].

The typical CIGS PV device is comprised of a stack of materials (described in detail in Section 1.3). A thin layer of CdS is deposited on the CIGS to help with the formation of a p-n junction. Experimental data and theory indicate that a Cu-poor CIGS region exists close to the interface between the CIGS and CdS [6, 9, 10]. It has been implied that the Cu-poor region forms an ordered vacancy compound (OVC) that has significant effects on device performance [11]. However, the connection between the measured properties of OVC layers and device performance have never been quantitatively evaluated. The main objective of this thesis is to investigate how variations in the electronic properties, including the thickness, band gap, electron affinity, doping, and defect concentrations of the CIGS/CdS interface region affect the overall device performance. Using numerical calculations and starting from a published baseline model, CIGS PV device performance will be predicted for a reasonable range of OVC layer parameters.

The primary hypothesis is that OVC layer electronic properties have a significant effect on device performance because it is located in the p-n junction and region of greatest photon absorption. This implies that relatively small variations in the electronic features of the OVC layer will have measurable effects on typical device metrics.

## 1.1 Background and History

The Sun is the most powerful energy source in the vicinity of the earth. It is a yellow star that emits about  $6.33 \times 10^7 \text{ W m}^{-2}$  radiation through nuclear fusion. With a total surface area of about  $6.09 \times 10^{15} \text{ m}^2$ , the total energy emitted is about  $3.85 \times 10^{23} \text{ W}$ . But only a fraction of that energy reaches earth and after going through the atmosphere only about  $925 \text{ Wm}^{-2}$  reaches the surface. Utilizing this clean energy has been a goal from the 18th century. Harvesting solar energy is mainly done by two methods. The first method is solar energy in the form of thermal energy. In recorded history, Swiss scientist, Horace de Saussure was the first to build a solar thermal collector [12]. The second method is generating DC current from solar energy through photovoltaic devices. In 1839, French physicist Alexander Edmond Becquerel was the first to demonstrate the photogalvanic effect [13]. Then in 1873 Willoughby Smith, an English engineer discovered photoconductivity in Selenium (Se), which sequentially led to producing the world's first solar cell by an American inventor, Charles Fritts [14]. In 1883 he created his solar cell by melting Se onto a metallic substrate and using a gold film as a top contact. The next major discovery happened in 1954 at Bell Labs in the USA - the discovery of p-n junction diodes, which built the foundation of the modern photovoltaic industry [15].

## 1.2 Generations of Photovoltaic Devices

Colloquially, there are three generations of PV devices. This categorization was carried out considering efficiency, cost, and technology. In first generation solar cells, there are two sub categories:

- a) Single crystal, based on Silicon or GaAs,
- b) Multi-crystal, based on Silicon,

Compared to multi-crystal solar cells, single crystal solar cells could achieve higher efficiencies but were very expensive to manufacture. Silicon based technologies (single and multi crystal) remain the most common types sold commercially. GaAs devices are more expensive but provide more power per unit area and are therefore popular for space applications.

With second generation solar cells, the most significant feature is that they are thin films. The absorber thickness is on the order of 1-5  $\mu\text{m}$ , whereas first generation Si cells are 100-500  $\mu\text{m}$  thick. These thin film cells absorb light much more efficiently due to the direct band-gap nature and larger absorption coefficient of the semiconductor [16]. Compared to the first generation, production cost is very low due to minimal material consumption and large-area, high throughput deposition. The most common solar cells in the second generation are:

- a) Amorphous Silicon (a-Si),
- b) Cadmium Telluride (CdTe),
- c) Copper Indium Gallium Selenide (CIGS).

Although second generation cells have lower efficiency, their cost per Watt value is quite competitive. They have also suffered from reliability issues which have improved over time. Due to the thin film nature, these solar cells could be used in many devices including windows, flexible devices, cars, and even in hand-held devices [17].

Relative to the second generation solar cells, third generation solar cells claim to provide much cheaper production cost which would lead to getting more effective cost per Watt values. The most significant technologies associated with third generation solar cells are:

- a) Dye-sensitized,
- b) Perovskite,
- c) Organic,
- d) Quantum dot.

Although this generation of solar cell technologies promise to provide cheaper production cost and a wide range of applications, current lab scale cells still report low efficiencies of around 10% except for some perovskite cells [18]. Furthermore, with the current state of this generation of

solar cells there are a few prevailing issues with some technologies, which include time consuming installation processes, short lifetime, stability, environmental concerns, and the requirement of large area to provide desirable power [19][20].

### 1.3 CIGS Devices

This section introduces the physical structure of CIGS solar cells and various characteristics of different layers of CIGS solar cells. These devices are called CIGS solar cells due to the absorber layer material and known for cost-effective power generation. Each layer in a CIGS solar cell serves a vital role in maximizing power conversion efficiency. The basic structure of the CIGS PV device is shown in Figure 1.1

Typical CIGS solar cells use soda lime glass as the substrate due to factors including soda lime being electrically neutral and a cost-effective material. Also, it is claimed to help Na diffusion from the glass to CIGS/CdS interface through grain boundaries in CIGS; which provides several benefits that enhance the efficiency [21] [7]. Other alternatives such as stainless steel and flexible polymers are also used as a substrate [17]. The Molybdenum (Mo) layer acts as the back contact in CIGS and helps to reflect light back into the CIGS layer. Also, Mo is preferred as a back contact for CIGS due to its low reactivity and for forming a low resistivity ohmic contact with CIGS [22]. The CIGS semiconductor acts as the photon absorber layer where the majority of electron-hole pair production happens and it has a thickness of about  $2 \mu m$ . CIGS has the chalcopyrite lattice structure with tetrahedral bond arrangement [23]. Being a direct band gap material, CIGS has a high absorption coefficient which makes it possible to use as an absorber layer in thin film solar cells. Figure 1.2 shows the chalcopyrite lattice structure for CIGS. Cu vacancies ( $V_{Cu}$ ) in the CIGS structure tend to make it p-type (acceptor type) [24].

Interchanging Ga and In atoms produces a different stoichiometry of CIGS,  $Cu(Ga_xIn_{1-x})Se_2$ , where  $x$  represents the Ga atomic fraction (GGI). Variation in Ga composition changes the lattice constant of CIGS, which changes the bandgap [21]. The relationship between the bandgap and Ga composition is further discussed in Section 3.3. The n-type CdS layer mainly serves two purposes, it acts as the protective layer for CIGS when sputtering ZnO, and CdS is helpful to create lattice

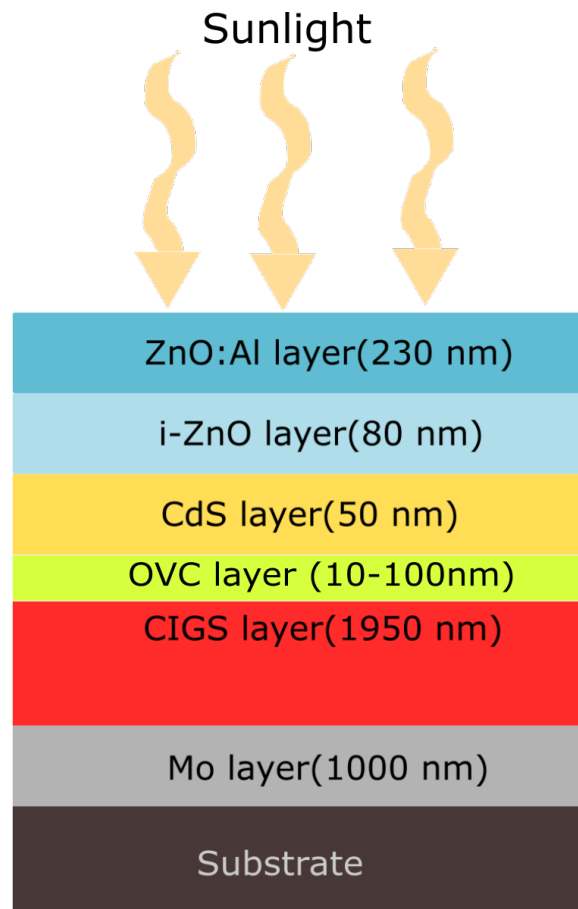


Figure 1.1 Basic structure of the CIGS PV device.

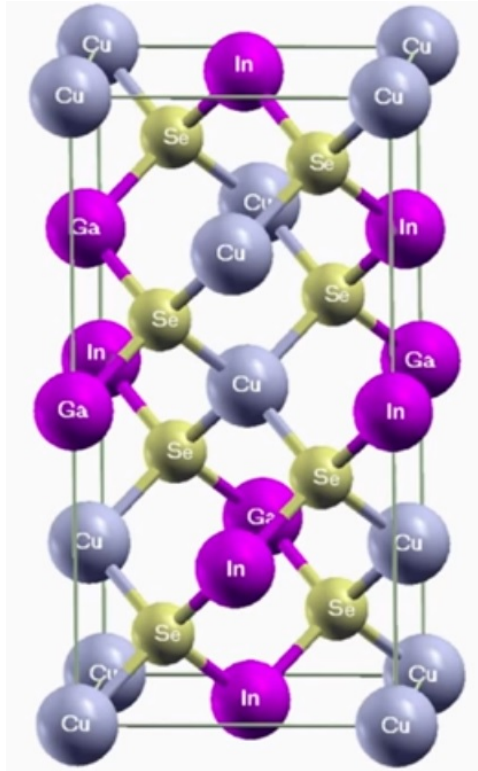


Figure 1.2 Lattice structure of CIGS [25].

matching between ZnO and CIGS for better efficiency [26]. The intrinsic, i-ZnO, layer acts as a high resistivity layer to reduce shunting but it must be very thin so that it does not affect the current collection. The transparent conductive ZnO layer doped with Al acts as the window layer and it collects the generated electrons for transport to metal contacts.

Commercial manufacturing of CIGS solar modules involves various deposition techniques for each layer. Figure 1.3 shows a schematic of how a typical module is monolithically interconnected by large area deposition and scribbling and lines represented by P1, P2, and P3. Typically, Mo is sputtered onto the substrate, then cut P1 is done by laser or mechanical scribbling. CdS and CIGS layers are then deposited using chemical bath deposition for CdS and co-evaporation of elements for CIGS. Next, the intrinsic ZnO layer is deposited using a sputtering technique, followed by second cut P2. After that, the transparent conductive ZnO layer is deposited using a sputtering technique. P1, P2, and P3 cuts serially connect CIGS solar cells completing the monolithic module. The P1 cut simply separates the Mo back contact of two cells, the P2 cut connects one solar cells

front contacts with the adjacent cell's back contact (Mo layer), and the P3 cut separates both cells front contacts to avoid short circuits [21, 27, 28]. In this way, large area thin film modules are produced.

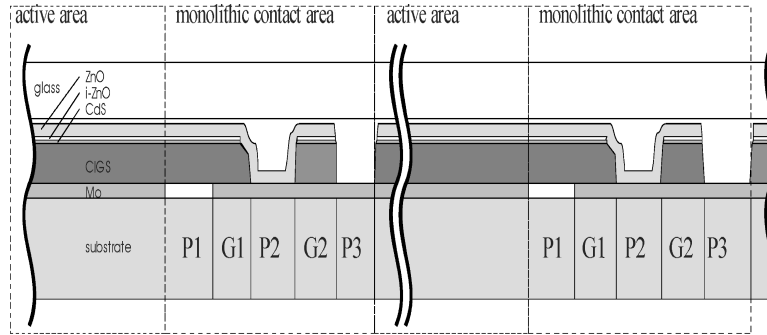


Figure 1.3 Monolithic interconnect structure of CIGS modules [27].

#### 1.4 Ordered Vacancy Compound Layer

As mentioned in the introduction, a Cu-poor layer is intentionally formed during CIGS deposition near the CIGS/CdS interface. That approach yields higher performance devices. The underlying reason, however, is unclear. In practice the non-stoichiometric layer (OVC layer) is included because it has been found that increasing copper results in device shunting, which is very detrimental to device operation [29]. Yet several publications suggest that the electronic properties of the OVC layer provides unique benefits in terms of doping and band alignment. This section provide specific information regarding the OVC layer from literature. The existence of a 15nm thick ordered vacancy compound layer (OVC) or an Ordered Defect compound layer (ODC) was suggested by analyzing results from the cross-over of dark and light current-voltage (JV) curves [9]. Formation of an OVC layer as result of stacking pairs of Ordered defect pairs (ODP) consisting of two Cu vacancies and an In or Ga on a Cu site ( $2V_{Cu} + (In, Ga)_{Cu}$ ) was predicted by atom probe tomography (APT) [10]. Transmission electron microscopy indicated the existence of a Cu-poor region within first 400 nm of the CIGS/CdS interface into bulk CIGS [10]. Analysis of the Cu concentration profiles of OVCs and CIGS suggested varying stoichiometry from  $Cu_2(InGa)_4Se_7$ ,  $Cu_3(InGa)_5Se_9$ , to conventional  $Cu(InGa)Se_2$  [10]. There are also reports of a 135-CIGS on Cu-poor CIGS surface [30–32]. In one experiment, a 135-CIGS stoichiometry

was intentionally deposited on 112 CIGS [33]. It was found that the Cu-poor 135-CIGS had a large band gap than 112-CIGS and combined structure had a larger band gap than 112-CIGS alone. High-angular annular dark field (HAADF) scanning transmission electron microscopy also provided evidence for the existence of a Cu-poor or OVC layer in the first 100 nm within the CIGS layer [6].

Although the exact nature of the Cu-poor/OVC layer is still debatable, different aspects were forwarded; some literature suggested the Cu-poor/OVC layer to be n-type doped [34], contrary to those models, the existence of an acceptor type (p-type) Cu-poor/OVC layer with high acceptor concentration ( $2.6 \times 10^{17} \text{cm}^{-3}$  [11]) was suggested. High vacancy defect densities have also been measured by positron annihilation spectroscopy [35]. In addition to stoichiometry and doping measurements, a valance band offset of about 0.2 eV between the CIGS and OVC layer has been suggested to improve device performance[36]. These electronic features and their observable effects are elaborated upon in this thesis, consistent with the objective described in the introduction.

Also due to acceptor defects having donor-like states expected to produce a valance band offset about 0.2eV closer to interface, as consequence of it efficiency expected to enhance by limiting holes traveling in to defect high interface region[6]. Further analysis about the effects of the OVC layer should be carried out to test whether electrical properties including the thickness, band gap, electron affinity, doping and defect concentrations of the OVC layer could enhance the overall efficiency of the PV device.

## CHAPTER 2 THEORY

This chapter focuses on the physics of PV devices and a numerical calculation method to solve the underlying equations. Further details on theoretical aspects and applications can be found in other published works [37],[38],[39] and the SCAPS software manual 2018 [40].

### 2.1 Semiconductor Equations

The equations involved in analyzing the semiconductor device are the Poisson equation [Eq. (2.1.1)] and current continuity equations [Eqs. (2.1.3)]. The relationship between electric potential ( $\psi$ ) and charge density ( $\rho$ ) depends on the electric permittivity ( $\epsilon$ ) and is given by,

$$\epsilon \nabla^2 \psi = -\rho. \quad (2.1.1)$$

For one-dimensional analysis Eq. (2.1.1) can be expressed,

$$\epsilon \frac{\partial^2 \psi}{\partial x^2} = -\rho = q(n - p + N_A - N_D + \frac{\rho_{def}}{q}), \quad (2.1.2)$$

where  $n, p, N_A$ , and  $N_D$  represent the electron, hole, acceptor, and donor concentrations, respectively. It should also be noted that, in this case, donors ( $N_D$ ) and acceptors ( $N_A$ ) are dopant concentrations and  $\rho_{def}$  represents the charged defect distribution.  $q$  is the elementary charge.

The following current continuity equations provide information about free charge carrier distributions inside the semiconductor. The time-dependent continuity equations include the difference of electron-hole (e-h) pair generation rate ( $G$ ) and recombination rate ( $U_{n,p}$ ) and are given by,

$$\frac{\partial J_n}{\partial x} - U_n + G = \frac{\partial n}{\partial t}. \quad (2.1.3)$$

$$\frac{\partial J_p}{\partial x} - U_p + G = \frac{\partial p}{\partial t}. \quad (2.1.4)$$

where  $J_n$  and  $J_p$  are electron and hole current densities respectively. For steady-state conditions time-dependent terms become zero. Hence, Eqs. (2.1.3) and (2.1.4) reduce to,

$$\frac{\partial J_n}{\partial x} - U_n + G = 0. \quad (2.1.5)$$

$$\frac{\partial J_p}{\partial x} - U_p + G = 0. \quad (2.1.6)$$

The current density inside the semiconductor is comprised of two components: drift and diffusion. Drift current is caused by the internal electric field and the diffusion component is caused by the charge concentration gradient within the semiconductor. The total current densities are then,

$$J_n = J_n^{drift} + J_n^{diffusion} \quad (2.1.7)$$

$$J_p = J_p^{drift} + J_p^{diffusion} \quad (2.1.8)$$

### 2.1.1 Drift Current

Drift current is defined for both electrons and holes using the following equations with charge concentrations ( $n$ ,  $p$ ), drift velocities ( $v_{d,n}$  and  $v_{d,p}$ ), mobilities ( $\mu_{n,p}$ ), and electric field ( $\xi$ ).

$$J_n^{drift} = qn v_{d,n} = qn \mu_n \xi \quad (2.1.9)$$

$$J_p^{drift} = qp v_{d,p} = qp \mu_p \xi \quad (2.1.10)$$

Mobility depends on scattering due to lattice parameters, ionized impurities, and grain boundaries. Hence, mobility could be defined using the mean free time ( $\tau_m$ ) or mean free path ( $\lambda_m$ ), and

effective masses of electron and holes ( $m_{e,h}^*$ )

$$\mu = \frac{q\tau_m}{m^*} = \frac{q\lambda_m}{\sqrt{3kTm^*}}. \quad (2.1.11)$$

Hence, Eqns. (2.1.9) and (2.1.10) can be modified as,

$$J_n^{drift} = q^2 n \frac{\lambda_m}{\sqrt{3kTm_n^*}} \xi. \quad (2.1.12)$$

$$J_p^{drift} = q^2 p \frac{\lambda_m}{\sqrt{3kTm_p^*}} \xi, \quad (2.1.13)$$

### 2.1.2 Diffusion Current

Diffusion current is due to charge migration from a region of higher concentration to a region with lower concentration. Flux of charge (electron and holes) ( $J_{n,p}$ ) can be explained by Fick's law, with diffusion coefficient given by  $D_{n,p}$ ,

$$J_n^{diffusion} = qD_n \frac{\partial n}{\partial x}, \quad (2.1.14)$$

$$J_p^{diffusion} = -qD_p \frac{\partial p}{\partial x}. \quad (2.1.15)$$

The diffusion coefficient is related to mobility by the Einstein relation where  $k$  and  $T$  represent Boltzmann constant and temperature,

$$D_{n,p} = \mu_{(n,p)} \frac{kT}{q}. \quad (2.1.16)$$

Given the above expressions for drift and diffusion current densities, the one-dimensional total current densities within semiconductor given by Eqns. (2.1.7) and (2.1.8) can be re-written as,

$$J_n = J_n^{drift} + J_n^{diffusion} = qn\mu_n\xi + qD_n \frac{\partial n}{\partial x}, \quad (2.1.17)$$

$$J_p = J_p^{drift} + J_p^{diffusion} = qp\mu_p\xi - qD_p\frac{\partial p}{\partial x}. \quad (2.1.18)$$

### 2.1.3 Generation of Electron-Hole Pairs

The dominant mechanism of free electron and hole generation in solar cells is intrinsic optical absorption of photons with energy greater than or equal to the absorber band gap. The generation rate [ $G(\lambda, x)$ ], at a distance  $x$  from the surface, for an incoming photon with wavelength  $\lambda$ , depends on the photon flux [ $N_{ph}(\lambda, x)$ ] and the absorption coefficient [ $\alpha(\lambda, x)$ ]. The generation rate can be written as,

$$G(\lambda, x) = \alpha(\lambda, x)N_{phot}(\lambda, x). \quad (2.1.19)$$

The photon flux decays exponentially in to the material according to  $N_{phot} = N_{phot0} \exp(-\alpha x)$ , where  $N_{phot0}$  is the incident flux. Integrating the generation rates with respect to wavelength for the spectral bandwidth provides the net generation rate  $G(x)$  at a distance  $x$  from the surface,

$$G(x) = \int_{\lambda_{min}}^{\lambda_{max}} \alpha(\lambda, x)N_{phot}(\lambda, x)d\lambda, \quad (2.1.20)$$

where the absorption coefficient,  $\alpha(\lambda, x)$ , depends on the material. For this research we used the following model for the absorption, which is appropriate for direct band gap semiconductors [37],

$$\alpha(\lambda, x) = A\sqrt{\frac{\hbar c}{\lambda} - E_g(x)}, \quad (2.1.21)$$

where  $A \sim 10^5 \text{ cm}^{-1}\text{eV}^{-\frac{1}{2}}$  is a model parameter,  $\hbar$ ,  $c$ , and  $\lambda$  represent reduced Planck constant, speed of light, and incoming photon wavelength. In thin films, multiple reflections must be considered because light absorption is typically not achieved in one pass. Calculating photon flux

$[N_{phot}(\lambda, x)]$  at  $x$  distance is handled by the following equation [40].

$$N_{phot}(\lambda, x) = N_{phot0}(\lambda, x)[1 - R_{Front}(\lambda)] \exp[-x\alpha(\lambda, x)] \frac{1 + R_{back}(\lambda) \exp[-2(d-x)\alpha(\lambda, x)]}{1 - R_{back}(\lambda)R_{int}(\lambda) \exp[-2d\alpha(\lambda, x)]} \quad (2.1.22)$$

where  $N_{phot0}(\lambda, x)$  is the photon flux at the illuminated surface,  $R_{Front}$  is the reflection at the front contact,  $R_{back}$  is the reflection at the back contact and  $R_{int}$  is the internal reflection at the front contact.

#### 2.1.4 Recombination

The reverse process of e-h pair generation is the recombination process. Recombination acts to restore equilibrium after a perturbation creates e-h pairs. In solar cells, recombination decreases device performance. Two main recombination categories can be identified:

- 1) band-to-band, and
- 2) recombination via defects.

Band-to-band recombination - Electrons in the conduction band exchange energy to a radiative or Auger process. In the radiative process a photon is emitted to conserve energy as an electron decreases its energy by shifting from the conduction band to the valence band. Direct recombination can also occur by the Auger process where an electron or hole loses energy through collision with another free carrier. The latter is more probable when the free carrier concentration is very high. The rate of radiative recombination is proportional to the product of electron and hole concentrations and can be calculated by following equation,

$$U_{radiative} = K(np - n_i^2), \quad (2.1.23)$$

where  $K$  is the radiative recombination constant and  $n_i$  is the intrinsic (equilibrium) carrier density. Radiative recombination is more preferable in direct bandgap semiconductor with  $K \sim 10^{-10} \text{cm}^3 \text{s}^{-1}$  compared to indirect with  $K \sim 10^{-15} \text{cm}^3 \text{s}^{-1}$ . However, in most thin film devices, defect levels in the band gap can be of sufficient densities to make non-radiative (trap-associated)

recombination the dominant mechanism, even though they have direct bandgaps.

Recombination through defects- non-radiative recombination of electrons and holes via defects, also known as Shockley-Read-Hall recombination, occurs through the release of multiple phonons.

The net rate of Shockley-Read Hall recombination is given by following equation,

$$U_{SRH} = \frac{\sigma_n \sigma_p v_{th} N_t (np - n_i^2)}{\sigma_n (n + n_i \exp(\frac{E_i - E_t}{kT})) + \sigma_p (p + n_i \exp(\frac{E_i - E_t}{kT}))}, \quad (2.1.24)$$

where  $N_t$  is the density of defects,  $\sigma_n$  and  $\sigma_p$  are the capture cross sections for electrons and holes,  $E_t$  is the defect energy level in the bandgap,  $v_{th}$  is the thermal velocity and  $E_i$  is the intrinsic energy level.  $U_{SRH}$  is a maximum when  $E_t = E_i$  and the above equation reduces to,

$$U_{SRH} = \frac{\sigma_n \sigma_p v_{th} N_t (np - n_i^2)}{\sigma_n (n + n_i) + \sigma_p (p + n_i)}. \quad (2.1.25)$$

## 2.2 Junction Formation

The equations and terms described thus far provide a general and basic description of charge transport in the most common semiconductor materials. A critical requirement for a PV device, however, is a built-in electric field that effectively separates e-h pairs. That field, or built-in potential,  $V_{bi}$ , is established by joining two materials with different Fermi levels with respect to vacuum. That can be accomplished with two semiconductors as a homojunction (for two of the same semiconductor with different doping levels) or a heterojunction (for two dissimilar materials), or as a metal/semiconductor Schottky junction. In CIGS devices, the CIGS/CdS interface forms a heterojunction where the CIGS is p-type (hole dominant) and the CdS layer is n-type (electron dominant).

In general, when two semiconductors with different Fermi levels (or free carrier densities) are brought into contact, charge flows between them until the Fermi level attains a constant, shared value, as shown in Figure 2.1.

The flow of free charge leaves behind fixed dopant charges (negative  $N_A$  or positive  $N_D$ ) thereby setting up a dipole and built-in field in accordance with the Poisson equation Eq. (2.1.1).

The free charges are balanced between diffusion due to the concentration gradient ( see Eq.2.1.15)and

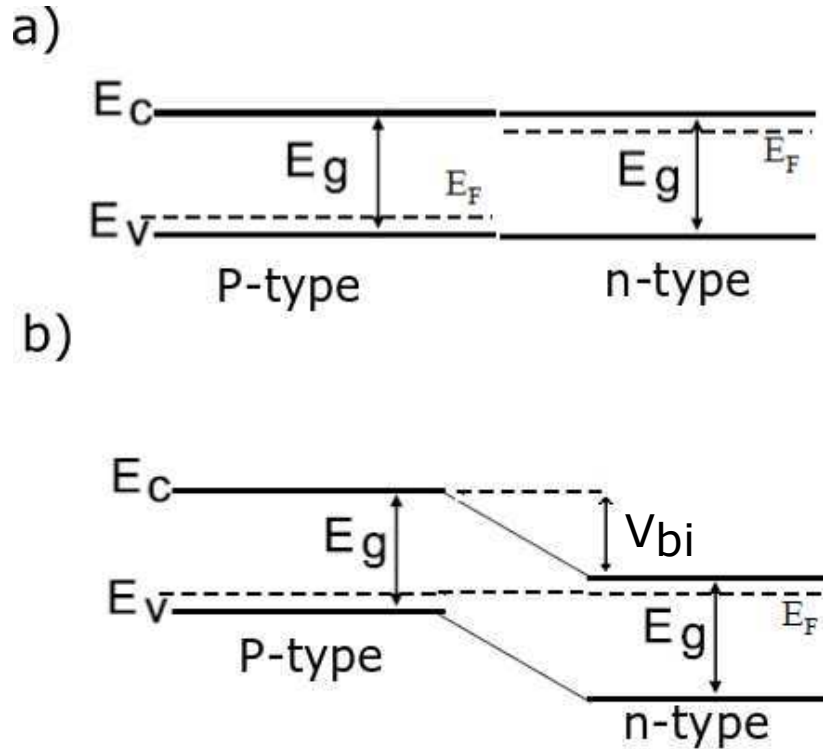


Figure 2.1 Formation of a pn junction, a) combining p-type and n-type semiconductors. b) balancing of the Fermi levels as the junction comes to equilibrium.

drift due to the electric field (see Eq. 2.1.9). The electrochemical potential, defined by the Fermi level, is flat and no charge flows. When a voltage bias is applied to one contact at the ends of the semiconductors or photons excite free carriers, equilibrium is disturbed, allowing the flow of electrons and holes. The flow is exponentially reduced in one direction due to the built-in voltage, causing rectifying (diode) behavior. A typical current-voltage relationship can be demonstrated by diode (or Shockley) equation [37],

$$J_D = J_s \left[ \exp\left(\frac{qV_D}{nkT}\right) - 1 \right] - J_L. \quad (2.2.1)$$

where  $V_d$  is the bias voltage,  $J_D$  is the diode current density,  $J_s$  is the saturation current density,  $J_L$  is the light induced current density  $T$  is the absolute temperature,  $k$  is the Boltzmann's constant, and  $n$  is the ideality factor varies from 1 to 2. An example of the  $J(V)$  characteristic for a solar cell and related performance metrics are provided in Section 3.5.

### 2.3 Interface States

Like most heterojunctions, the CIGS/CdS interface is prone to a high density of defect states that can act as surface recombination centers and charge centers that affect charge transport and the built-in field. The interface defects come about due to lattice mismatch between the materials, impurities during deposition, and incomplete or wrong bonds at the material surfaces. Heterojunctions also have discontinuities in electronic properties, such as band gap,  $E_g$ , electron affinity,  $\chi$ , and permittivity,  $\epsilon$ . The extension of the homojunction model to include those discontinuities is called the Anderson model [41]. An important aspect of this work is the discontinuity in  $\chi$  which leads to differences in the conduction and valence bands, called band off-sets defined as,

$$\Delta E_c = -\chi_2 + \chi_1 \quad \text{and} \quad \Delta E_v = \chi_2 - \chi_1 + E_{g2} - E_{g1}. \quad (2.3.1)$$

The subscripts 1 and 2 represent semiconductor 1 and 2 in the heterojunction. The schematic of a heterojunction in Figure 2.2 shows the band offset at OVC/CdS interface. By increasing the band gap at the interface, recombination at the interface states (short lines in the bandgap) decreases.

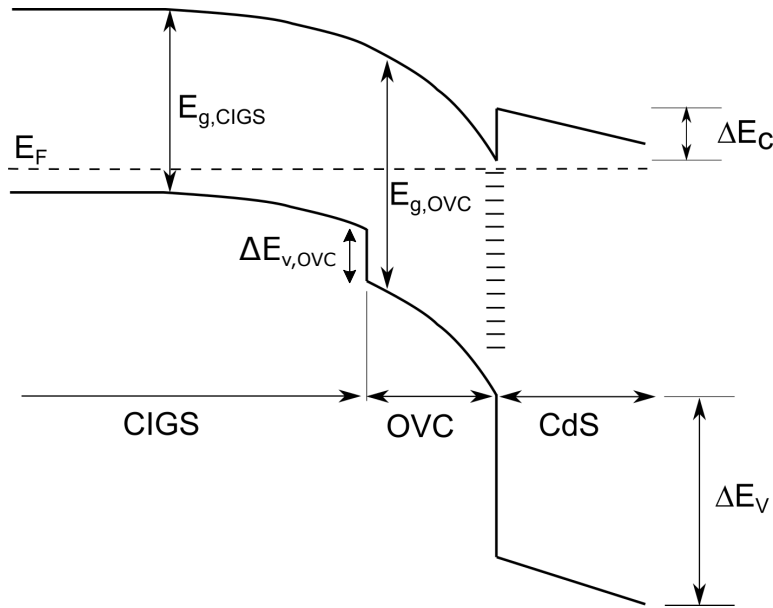


Figure 2.2 A figure of a simple heterojunction showing the conduction and valence band offsets and  $\chi$  and  $E_g$ .

The ideal model is not typically realized in practice. Interdiffusion of elements between the two semiconductors causes a smearing of the properties rather than discontinuities. Interface states that are difficult to isolate and measure are also common. In CIGS/CdS devices, the formation of an OVC layer has been observed, as discussed in Section 1.4. In practice, the OVC layer is caused by the intentional reduction of copper content during deposition of that region of the device. Increasing the copper content to stoichiometric levels often results in deleterious effects, such as current shunting which circumvents the built-in potential. This work considers the electronic properties of the interface region of the CIGS/OVC/CdS layer.

## CHAPTER 3 METHODOLOGY

The methodology in this work entailed numerical calculations to solve the coupled semiconductor equations, establishment of a baseline model by comparison to relevant data, and extension of that baseline model to include an OVC layer with reasonable parameter values informed by a literature review.

### 3.1 Numerical Calculations

Numerical simulations were carried out for analyzing the effects of electrical properties of the OVC layer towards the device efficiency; SCAPS 1D software was used to carry out numerical simulations [42],[40]. SCAPS 1D is an open-source, one-dimensional solar cell simulation software. This program was developed at the Department of Electronics and Information Systems of the University of Gent, Belgium. Numerical calculations were carried out by using the finite difference method to solve the coupled semiconductor equations discussed in Chapter 2, repeated here for convenience.

$$\epsilon \frac{\partial^2 \psi}{\partial x^2} = q(n - p + N_A - N_D + \frac{\rho_{def}}{q}) \quad (3.1.1)$$

$$\frac{\partial J_n}{\partial x} - U_n + G = 0 \quad (3.1.2)$$

$$\frac{\partial J_p}{\partial x} - U_p + G = 0 \quad (3.1.3)$$

where  $\psi$ ,  $n$ ,  $p$ ,  $N_A$ , and  $N_D$  represent the electric potential, electron, hole, acceptor, and donor concentrations, respectively. The electron ( $J_n$ ) and hole ( $J_p$ ) current densities along with the recombination ( $U_n, U_p$ ) and generation rates ( $G$ ), were also elaborated upon in Chapter 2. It should also be noted that, in this case, donors  $N_D$  and acceptors  $N_A$  are considered as the dopant concentrations and  $\rho_{def}$  represents the defect distribution.

### 3.2 Baseline Models

As the first step, four models (A-D) were developed without the OVC layer (refer to Figure 1.1) to build suitable baseline models with data provided in [43]. All model parameters are indicated in Table 3.1, and the major differences among the four models were different defect configurations. Numerical analyses were carried for both single and double graded Ga compositions, as discussed in Section 3.3. Therefore a total of eight baseline models were considered.

Model A had the simplest defect configuration of midgap donor defects with constant concentration  $N_t = 2 \times 10^{12} \text{ cm}^{-3}$ . Model B had donor type midgap defects with Ga-dependent concentration. Model C was defined with a constant donor type midgap defect concentration along with an additional metastable defect profile. Model D was defined with Ga-dependent donor type midgap defect with metastable defects. Numerical simulations were carried out to calculate current-voltage (JV) and external quantum efficiency (EQE) curves. Then, our results were compared with the results published in [43]. Despite the different defect configurations, numerical simulation results (JV and EQE curves) indicated all four models behaved similarly to each other (see results in Chapter 4). Therefore, Model A, which had the simplest defect configuration, was selected for further analysis of OVC layer effects on device efficiency. interface state were included at the CIGS/CdS interface. The concentration was  $N_{it} = 10^{-15} \text{ cm}^{-2}$  at an energy level in the middle of CIGS band gap. Electron and hole capture cross-sections were  $\sigma_n = 5 \times 10^{-13} \text{ cm}^2$  and  $\sigma_p = 5 \times 10^{-15} \text{ cm}^2$ , respectively [43].

When an OVC layer is added, states are modified to separate the OVC/CdS interface according to Ref.[44]. In that case,  $\sigma_n = 10^{-18} \text{ cm}^2$  and  $\sigma_p = 10^{-13} \text{ cm}^2$  at defect energy level of 0.65 eV above the CIGS valence band maximum. The concentration was  $N_{it} = 10^{12} \text{ cm}^{-2}$ . Although these parameter values were not substantiated experimentally, they are used here for comparison to the previous models.

### 3.3 Band-gap Grading

By tuning the Ga composition (GGI ratio or ratio of Ga for total Ga and In) in CIGS material, a graded band structure can be achieved. In this section, the relationships between GGI ratio, band gap ( $E_g$ ), and electron affinity ( $\chi$ ) are analyzed. The following expressions provide the dependence of  $E_g$  and  $\chi$  on Ga content [43][45].

$$GGI = y = \frac{[Ga]}{[Ga] + [In]} \quad (3.3.1)$$

$$E_g = 1.01 + 0.626(y) - 0.167(y - y^2) \quad (3.3.2)$$

$$\chi = 4.5 - 0.626(y) + 0.167(y - y^2) \quad (3.3.3)$$

Figure 3.1 shows the dependence of  $E_g$  and  $\chi$  on double and single graded Ga compositions. Double graded composition follows a “V” like shape and the first half of the “V” shape is called the front grading and latter part is referred as back grading. Double graded Ga composition was claimed to provide improved  $V_{oc}$  with front grading [46, 47]. Back grading claimed to provide higher  $J_{sc}$  over single graded Ga composition [46, 47].

Table 3.1 Baseline model parameters[43].

Layer Parameter	ZnO : Al	i-ZnO	CdS	CIGS
Thickness (nm)	230	80	50	1950
Band Gap (eV)	3.3	3.3	2.4	1.0-1.6 (Ga dep.)
Electron affinity (eV)	4.4	4.4	4.2	4.5-3.9 (Ga dep.)
Rel. permittivity	9	9	5.4	13.6
CB DOS (cm <sup>-3</sup> )	$3 \times 10^{18}$	$3 \times 10^{18}$	$1.3 \times 10^{18}$	$6.8 \times 10^{17}$
VB DOS (cm <sup>-3</sup> )	$1.7 \times 10^{19}$	$1.7 \times 10^{19}$	$9.1 \times 10^{19}$	$1.5 \times 10^{19}$
Electron mobility (cm <sup>2</sup> V <sup>-1</sup> s <sup>-1</sup> )	100	100	72	100
Hole mobility (cm <sup>2</sup> V <sup>-1</sup> s <sup>-1</sup> )	31	31	20	13
Doping (cm <sup>-3</sup> )	$10^{20}$	$10^{17}$	$5 \times 10^{17}$	$7 \times 10^{15}$ (A,C) $1.1 \times 10^{16}$ (B,D)
Mid gap defects (cm <sup>-3</sup> )	$10^{16}$	$10^{16}$	$10^{12}$	$2 \times 10^{12}$ (A,C) $2 \times 10^{12} - 1 \times 10^{14}$ (B,D)(Ga dep.)
Metastable defect con. (cm <sup>-3</sup> )	None	None	None	$9 \times 10^{15}$ (C,D)

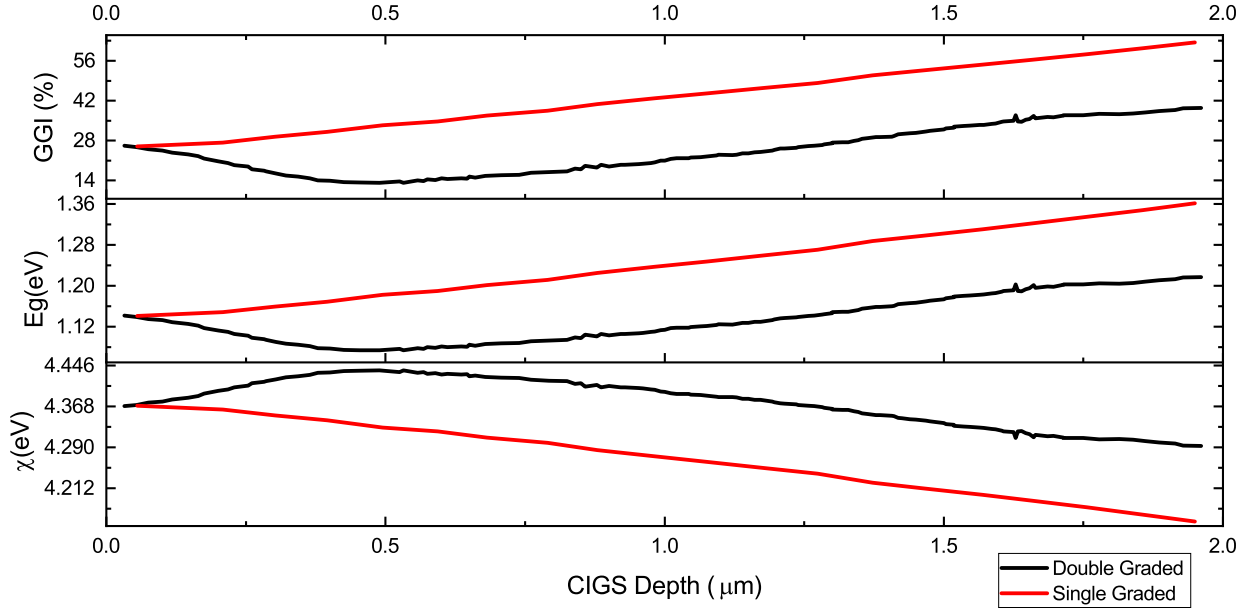


Figure 3.1 Graded band gap (center panel) and electron affinity (bottom panel) based on measured Gallium profiles[43] for single (red) and double graded (black) cases.

### 3.4 Model A with OVC Layer

An additional layer having the proposed properties of the OVC layer was introduced into Model A in between the CIGS and CdS layers, as shown in Figure 1.1. Numerical simulations were carried out with various properties of the OVC layer shown in Table 3.2. Meanwhile other properties including effective density of state, mobilities, and relative permittivity were kept same as shown in Table 3.1. The given variable parameter ranges in Table 3.2 can be reasoned by published literature. Variable OVC parameter values were informed by the literature and are provided in Table II. The thickness,  $d_{OVC}$ , was reported as 15 nm [9], 50–100 nm [48], and up to 400 nm [10]. Hence, we used a range of 0-100 nm for the OVC thickness. The band gap range was informed by optical measurements on OVC samples and photoelectron spectroscopy which indicated that the OVC band gap is ~1.3 eV; typically larger than the adjacent bulk absorber [41, 49]. Band gap variations are process sensitive and values up to 1.6 eV have been observed [48]. We used a band gap range of 1.1-1.6 eV because it also considers the approximate extremes of CIS to CGS band gaps. The results in Refs. [49] and [50] also suggested that the OVC valence band is below that

of the CIGS by about 0.2 eV. We consider the effects of band offsets by including a wide range of OVC electron affinity.

Table 3.2 Variable parameters in OVC layer and CIGS composition.

Parameter	Symbol/Unit	Range
OVC thickness	$d_{OVC}$ (nm)	0 – 100
OVC affinity	$\chi_{OVC}$ (eV)	3.8 – 4.6
OVC band gap	$E_{g,OVC}$ (eV)	1.1 – 1.6
OVC acceptors	$N_{A,OVC}$ (cm <sup>-3</sup> )	10 <sup>12</sup> – 10 <sup>20</sup>
OVC deep defects	$N_{t,OVC}$ (cm <sup>-3</sup> )	10 <sup>12</sup> – 10 <sup>20</sup>
CIGS composition grading		double/single graded

### 3.5 J-V Characteristic Curve

Current vs voltage (IV) characteristic curves can be plotted for dark and illuminated conditions. Using I-V curves, it is possible to calculate the total efficiency of a device by extracting values for open circuit voltage ( $V_{oc}$ ), short circuit current ( $I_{sc}$ ), and fill factor ( $FF$ ), which measures how much the I-V curve deviates from the ideal I-V curve. Figure 3.2 shows an I-V curve for a typical solar cell in dark and light. These are often presented as current density vs voltage (JV) curves. The area of the dark color rectangle represents the maximum power ( $P_m$ ) generated by the solar cell. At the maximum power generating point, voltage and current values are represented by  $V_m$  and  $I_m$ , respectively. The maximum power point can be calculated by the area under the curve.

$$P_m = I_m V_m = FF I_{sc} V_{oc} \quad (3.5.1)$$

Efficiency ( $\eta$ ) is calculated by,

$$\eta = \frac{P_m}{P_{in}} = \frac{I_m V_m}{I_{sc} V_{oc}} = \frac{FF I_{sc} V_{oc}}{P_{in}} \quad (3.5.2)$$

### 3.6 EQE Curves

Quantum Efficiency (QE) measurements for a solar cell measures the photo sensitivity of a device with respect to wavelength. There are two types of QE measurements, External Quantum

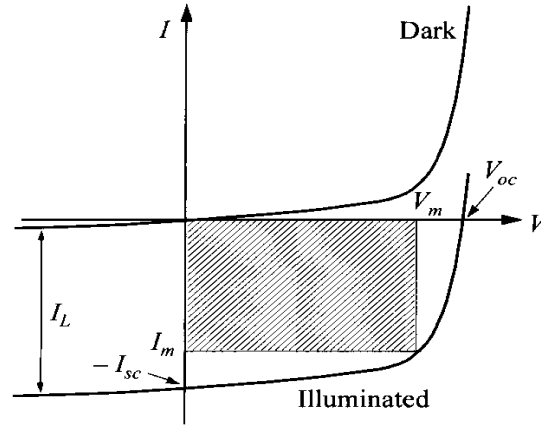


Figure 3.2 I-V curve for a typical solar cell in dark and light [37].

Efficiency (EQE) and Internal Quantum Efficiency (IQE). EQE measures the ratio of the number of charge carriers collected by the solar cell to the number of incident photons with respect to photon wavelength. IQE measures the ratio of the number of charge carriers collected by the solar cell to the number of absorbed photons with respect to photon wavelength.

In our analysis we calculated the EQE curves, which are sensitive to both absorption (1-Reflection) and charge collection. For the optical absorption in our models we used  $\alpha(\lambda, x) = A\sqrt{h\nu - E_g(x)}$  (see Eq. 2.1.21) where  $\nu$  is incoming photon frequency,  $E_g$  is the band gap of the material, and  $A$  is the modeling parameter. With trial and error we determined the  $A = 5 \times 10^4 \text{ cm}^{-1}(\text{eV}^{-\frac{1}{2}})$  for the best matching with the published EQE curves in [43]. Initial calculations without a reflectivity profile (with a 100% transmission) provided results with near 100% EQE for a region of wavelengths, which is inconsistent with observations. We therefore incorporated the reflectivity profile from Frisk et.al [43] in our device models, as shown in Figure 3.3. This provided optimal matching of EQE data, as described in Section 4.1.2.

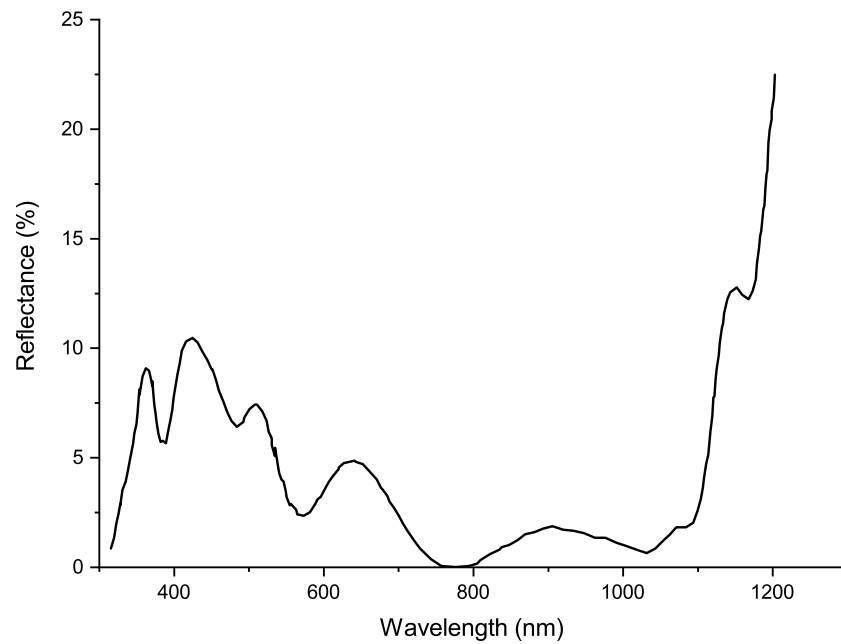


Figure 3.3 Reflectivity profile introduced for front contact [43].

## CHAPTER 4 RESULTS

### 4.1 Results for Baseline Models

In this section, output results for the baseline models described in Chapter 3 are presented. Eight baseline models were created and current-voltage (JV) curves and external quantum efficiency (EQE) calculations were carried out. These results were compared to the reference models and data from a typical CIGS cell in Ref. [43].

#### 4.1.1 JV Curves

JV calculations were conducted for double graded composition at working point conditions of  $T = 300$  K and light of  $1000 \text{ W/m}^2$  intensity with the AM 1.5G spectrum [43]. Table 4.1 lists the performance metrics of the reference models and data (denoted as "Ref.") and our calculations (denoted as "Model").

All four baseline models demonstrated almost identical current-voltage curves, as shown in Figure 4.1. The performance metrics extracted from the JV curves are provided in Tables 4.1 and 4.2 for double and single graded compositions, respectively. Compared with the published data Ref. [43], our models followed very similar curves, except all our models have higher  $\eta$ . The discrepancies are likely due to a slightly lower defect concentration used in our models, which would result in higher  $V_{oc}$  and  $J_{sc}$ . Differences in FF could be due to different series resistance assumed but not reported in the Ref. [43] calculations. The series resistance of the device is reflected in the slope of the JV curve for  $V > 600$  mV. Regardless, all of the calculations produce nearly 20% efficient devices and Model A is sufficient for studying the effects of the OVC layer.

#### 4.1.2 EQE Curves

EQE calculations for all four models with double graded composition discussed in Section 3.2 are shown in Figure 4.2. Similar to the JV curves, all four baseline models demonstrated almost identical EQE curves and also when compared with published data from models in [43]. Also, it should be noted that by introducing the measured reflectance profile from [43] (see Figure

Table 4.1 Performance metrics of reference models [43] and our calculations for models A-D with double graded composition.

Model	$V_{oc}$ (mV)	$J_{sc}$ (mA cm <sup>-2</sup> )	FF (%)	$\eta$ (%)
Model A	697	38.33	76.79	20.54
Model B	699	39.31	75.63	20.79
Model C	704	38.85	75.79	20.74
Model D	693	38.24	77.87	20.64
Ref. A	680	38.1	75.7	19.6
Ref. B	681	38.0	75.4	19.5
Ref. C	687	37.8	75.6	19.6
Ref. D	685	37.6	75.8	19.5
Ref. cell	685	36.8	75.9	19.1

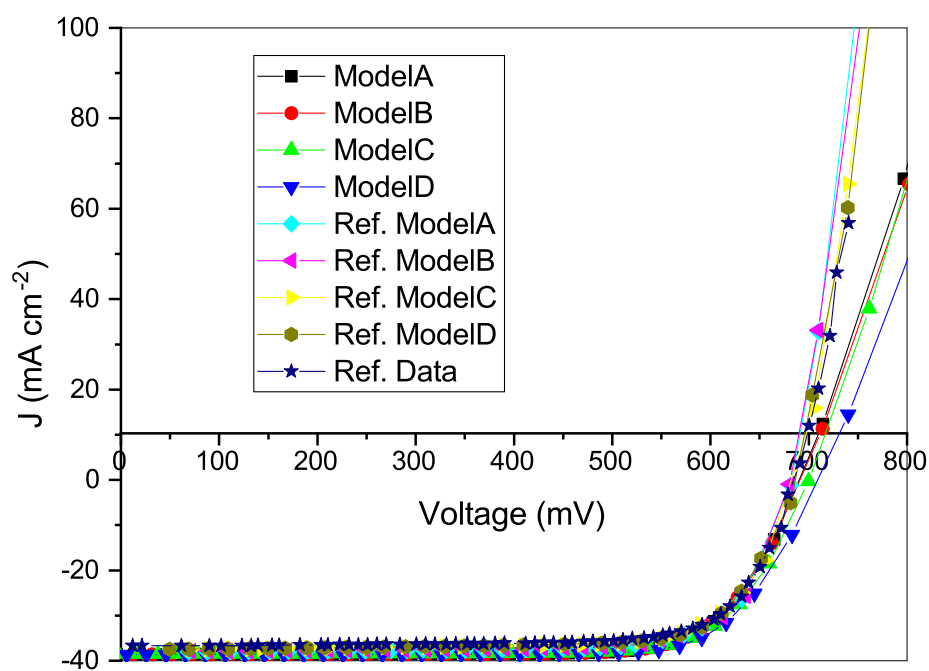


Figure 4.1 JV curves for all our models and reference models from [43] with double graded composition. Measured data from a reference cell is also indicated as Ref. Data.

Table 4.2 Performance metrics of reference models [43] and our calculations for models A-D with single graded composition. The Ref. cell had double graded composition.

Model	$V_{oc}$ (mV)	$J_{sc}$ (mA cm <sup>-2</sup> )	FF(%)	$\eta$ (%)
Model A	830	34.85	77.47	22.42
Model B	828	35.84	77.24	22.95
Model C	835	35.46	76.33	22.62
Model D	817	34.8	81.45	23.18
Ref. A	757	34.5	78.9	20.6
Ref. B	746	35.1	79.4	20.8
Ref. C	747	34.6	79.3	20.5
Ref. D	739	35.0	79.7	20.6
Ref. cell	685	36.8	75.9	19.1

3.3), ripples on the top of the EQE curves were obtained. These ripples are due to the wavelength dependent interference effects of the thin layers and multiple reflections within each layer. The high level of EQE in the wavelength range between 520 nm and 1100 nm is due to minimal reflectivity and efficient light absorption and carrier collection in the CIGS absorber. The steep drop-off after 1100 nm is due to photon energy being less than the CIGS band-gap. Below  $\lambda=520$  nm, absorption is primarily in CdS layer ( $E_g = 2.4$  eV = 517 nm). Poor carrier collection (lower EQE) is due to higher recombination rates in CdS. Below  $\lambda=375$  nm, absorption occurs in the ZnO layer ( $E_g = 3.3$  eV = 375 nm).

#### 4.2 Effects of OVC Doping, Deep Defect Density, and Thickness

Extended Model A with an OVC layer in between CIGS and CdS was used to investigate the influence of different electrical properties (see Section 3.4) on efficiency. In this section we study how OVC shallow acceptor density (doping), deep defects density, and thickness of the OVC layer affect the device efficiency. Calculations were carried out for different combinations of OVC acceptor density from  $10^{12}$  cm<sup>-3</sup> to  $10^{20}$  cm<sup>-3</sup>, donor type mid-gap defect density from  $10^{12}$  cm<sup>-3</sup> to  $10^{20}$  cm<sup>-3</sup>, and OVC layer thicknesses at 0.01  $\mu$ m, 0.05  $\mu$ m, and 0.1  $\mu$ m. Other OVC parameters were:  $E_{g,OVC} = 1.3$  eV and  $\chi_{OVC} = 4.3$  eV. We also considered single and double graded composition profiles for our calculations (see Section 3.3). Figure 4.3 shows the calculations carried out with double graded composition grading for different thicknesses of the OVC layer:

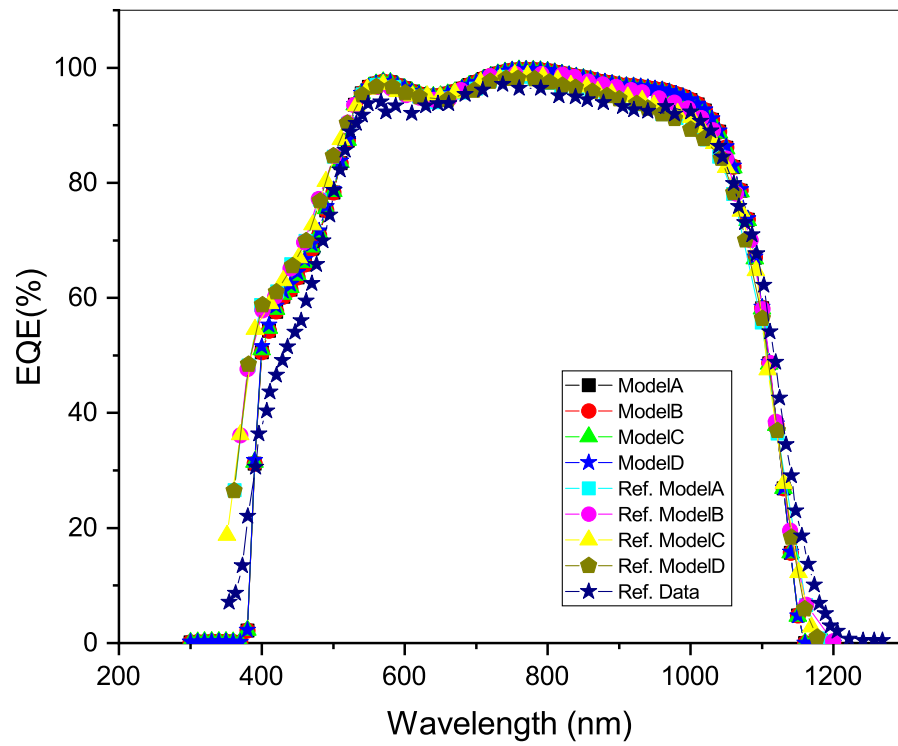


Figure 4.2 QE curves for all our models and reference models from [43] with double graded composition. Measured data from a reference cell is also indicated as Ref. Data.

(a)  $0.01\ \mu\text{m}$ , (b)  $0.05\ \mu\text{m}$  and (c)  $0.1\ \mu\text{m}$ . Figure 4.4 shows the calculations carried out with single graded composition grading for different thickness of the OVC layer: (a)  $0.01\ \mu\text{m}$ , (b)  $0.05\ \mu\text{m}$  and (c)  $0.1\ \mu\text{m}$ . When analyzing Figures 4.3 and 4.4, we observe almost identical behavior, except that the single graded model indicated higher efficiency values. The maximum efficiencies were 20.1% and 21.8% for double and single graded compositions, respectively. Similar observations of single graded band having higher efficiencies are mentioned in Ref. [51]. Both Figures 4.3 and 4.4 indicate that mid-gap donor defects density ( $N_{t,OVC}$ ) did not affect efficiency for the thinnest OVC layer of 10 nm. However, as the thickness increased, higher mid-gap defect densities caused a decrease in efficiency. That is because as the thickness increases, the total recombination increases, which results in  $V_{oc}$  and efficiency loss. Specifically, our result show that  $N_t \geq 10^{17}\ \text{cm}^{-3}$  in the OVC layer can be detrimental to device performance. Efficiency loss due to shallow acceptor density ( $N_{A,OVC}$ ) was more apparent for all thicknesses. For thicknesses of 10 nm, 50 nm, 100 nm, respectively, rapid efficiency decline was apparent for  $N_A \geq 10^{19}\ \text{cm}^{-3}$ ,  $2 \times 10^{17}\ \text{cm}^{-3}$ , and  $10^{17}\ \text{cm}^{-3}$ . The rapid decline at the high acceptor densities is due to negative charge in the OVC layer that becomes greater than the positive charge in the n-type CdS layer, resulting in a distorted electric field. The distorted band bending that occurs at high  $N_{A,OVC}$  values can be observed in Figure 4.8 (c). In that case, most of the efficiency loss is through  $J_{sc}$ . The efficiency dependence on  $N_{A,OVC}$  can be seen more clearly in Figures 4.5 (a) and (b) for double and single graded compositions, respectively. In those figures, a defect value of  $N_{t,OVC} = 10^{12}\ \text{cm}^{-3}$  was assumed. Figure 4.5 also shows more clearly how OVC thickness affects efficiency for various shallow acceptor densities. That result is clarified further in Figure 4.6, which shows line graphs of efficiency verses thickness for (a) double graded, and (b) single-graded CIGS band gaps. Figure 4.5 and 4.6 both indicate that thinner OVC layer and single graded CIGS composition result in higher efficiencies. The reasons for efficiency loss can be understood by studying how the metrics of  $V_{oc}$ ,  $J_{sc}$  and  $FF$  change within the parameter space, as shown in Figures 4.7 (a), (b), and (c). We recall that efficiency can be expressed as  $\eta = \frac{V_{oc}J_{sc}FF}{P_{in}}$ . From Figure 4.7, it is evident that  $J_{sc}$  is most closely correlated with drastic efficiency loss at high shallow acceptor density. Figure 4.7 (a)

shows that some  $V_{oc}$  increase can also be observed in region where the efficiency decreases. These drastic changes occur when the built-in electric field exists predominately in CdS layer as shown in Figure 4.8(c).

### 4.3 Effect of Band Off-Set

As discussed in Chapter 1, hypotheses were suggested in Ref. [6] that a p-type OVC layer could result in a valence band off-set by lowering the valence band maximum, which would enhance the overall device efficiency by increasing  $V_{OC}$ , reducing the recombination, and pushing away holes entering the defect rich junction. Results from our Model A with p-type doping demonstrated a similar band offset of about 0.2 eV. However, contrary to the hypothesis, our results in Section 4.2 for single-graded and double-graded compositions indicated that such an OVC layer did not enhance the device efficiency, yet it could reduce the overall efficiency if the OVC p-type doping or thickness was too large. Figure 4.8 shows the band structure close to the interface of the CIGS and CdS layers for different OVC layer thicknesses and doping densities. Other OVC parameters are  $E_{g,OVC}=1.3$  eV,  $\chi_{OVC}= 4.3$  eV, and  $N_t=10^{12}\text{cm}^{-3}$ .

Figure 4.8 (a) shows a valence band offset ( $\Delta E_{V,OVC}$ ) of 0.2 eV for 10 nm thick OVC layer and with OVC acceptor doping  $10^{18} \text{ cm}^{-3}$ . This model maintains the band bending within the CIGS layer and keeps its efficiency around 20%. In Figure 4.8 (b) it also shows a valence band offset of 0.2 eV for 100 nm thick OVC layer and with less acceptor doping of  $10^{16} \text{ cm}^{-3}$ . In that case, the band bending is maintained inside the CIGS layer and efficiencies are around 20%. In Figure 4.8 (c), the valence band off-set of 0.2 eV is still present, but the 100 nm - thick OVC layer with  $10^{18} \text{ cm}^{-3}$  doping results in a conduction band hump. It can be observed in Figure 4.8 (c) that most of the built-in potential drops across the CdS layer, resulting in almost no depletion region in CIGS layer and, consequently, very poor carrier collection. That also explains the low  $J_{sc}$  value for this case discussed with respect to Figure 4.7 (b).

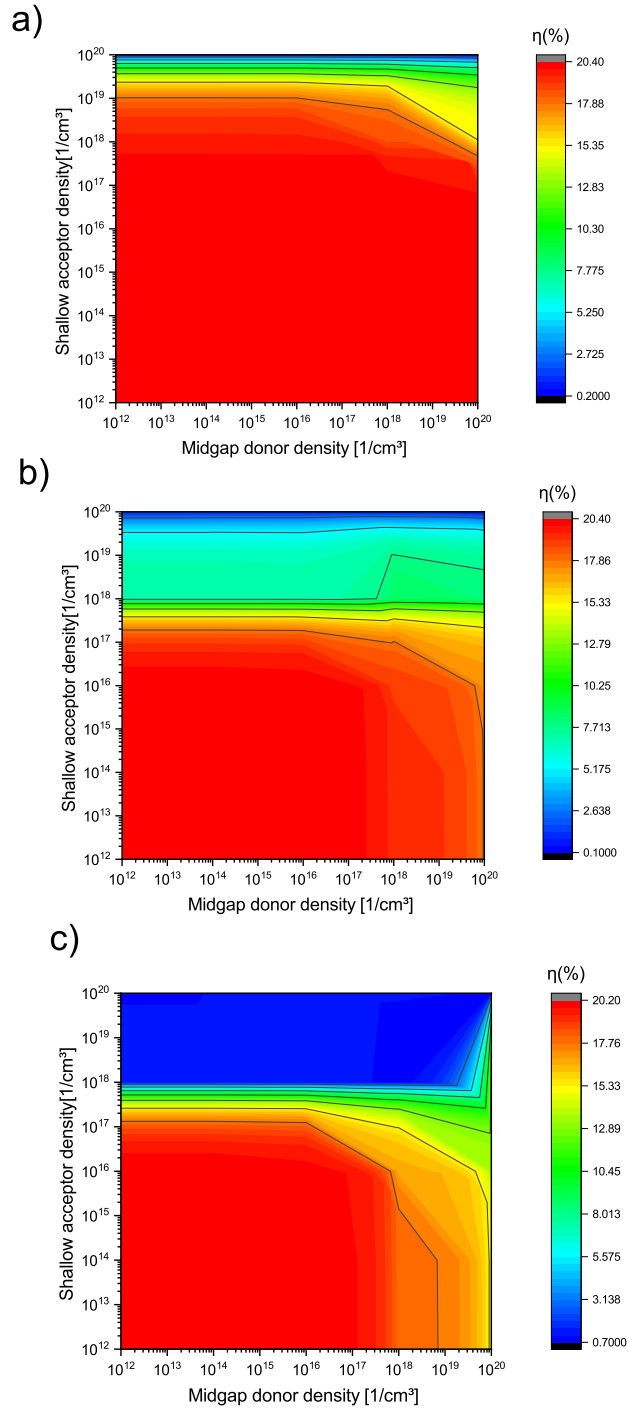


Figure 4.3 Efficiency dependence on mid-gap donor density and shallow acceptor density in the OVC layer for OVC thicknesses of (a) 10 nm, (b) 50 nm, and (c) 100 nm. These calculations assume the double graded Ga profile (see Figure 3.1).

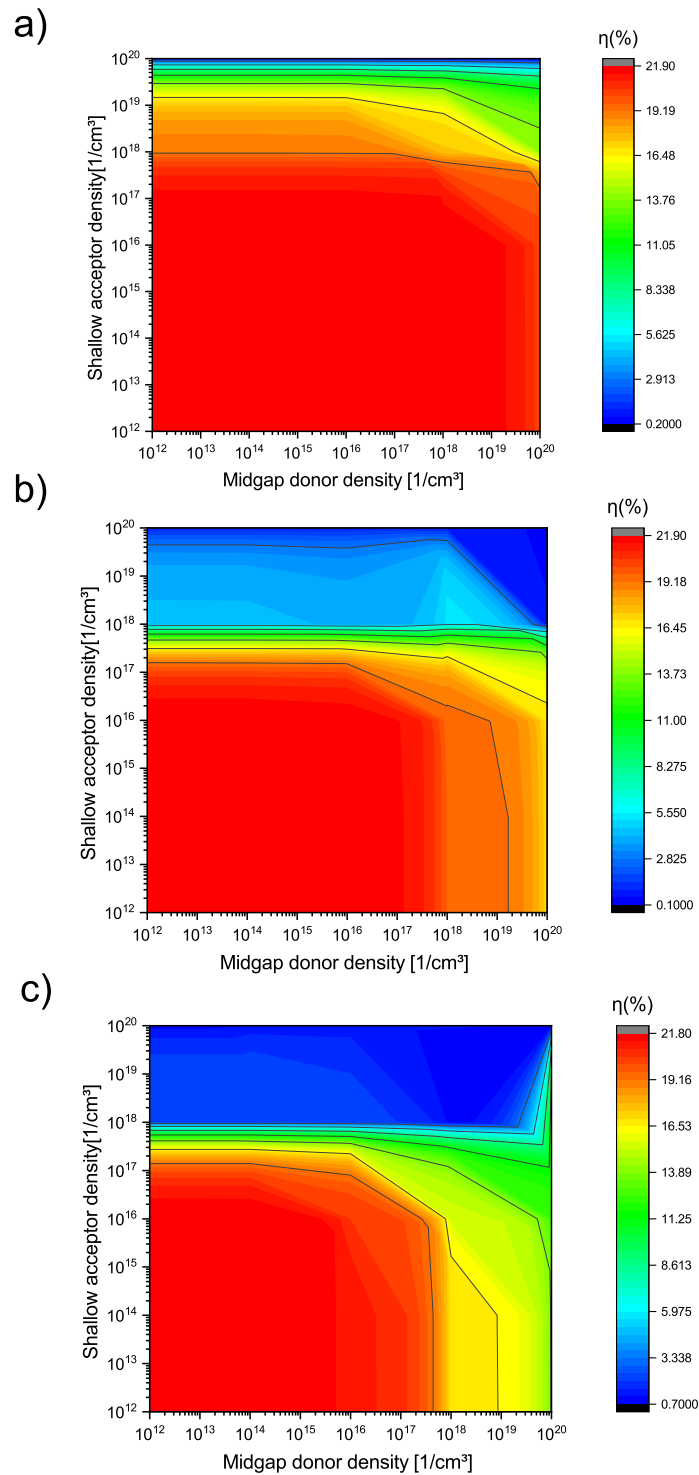


Figure 4.4 Efficiency dependence on mid-gap donor density and shallow acceptor density in the OVC layer for OVC thicknesses of (a) 10 nm, (b) 50 nm, and (c) 100 nm. These calculations assume the single graded Ga profile (see Figure 3.1).

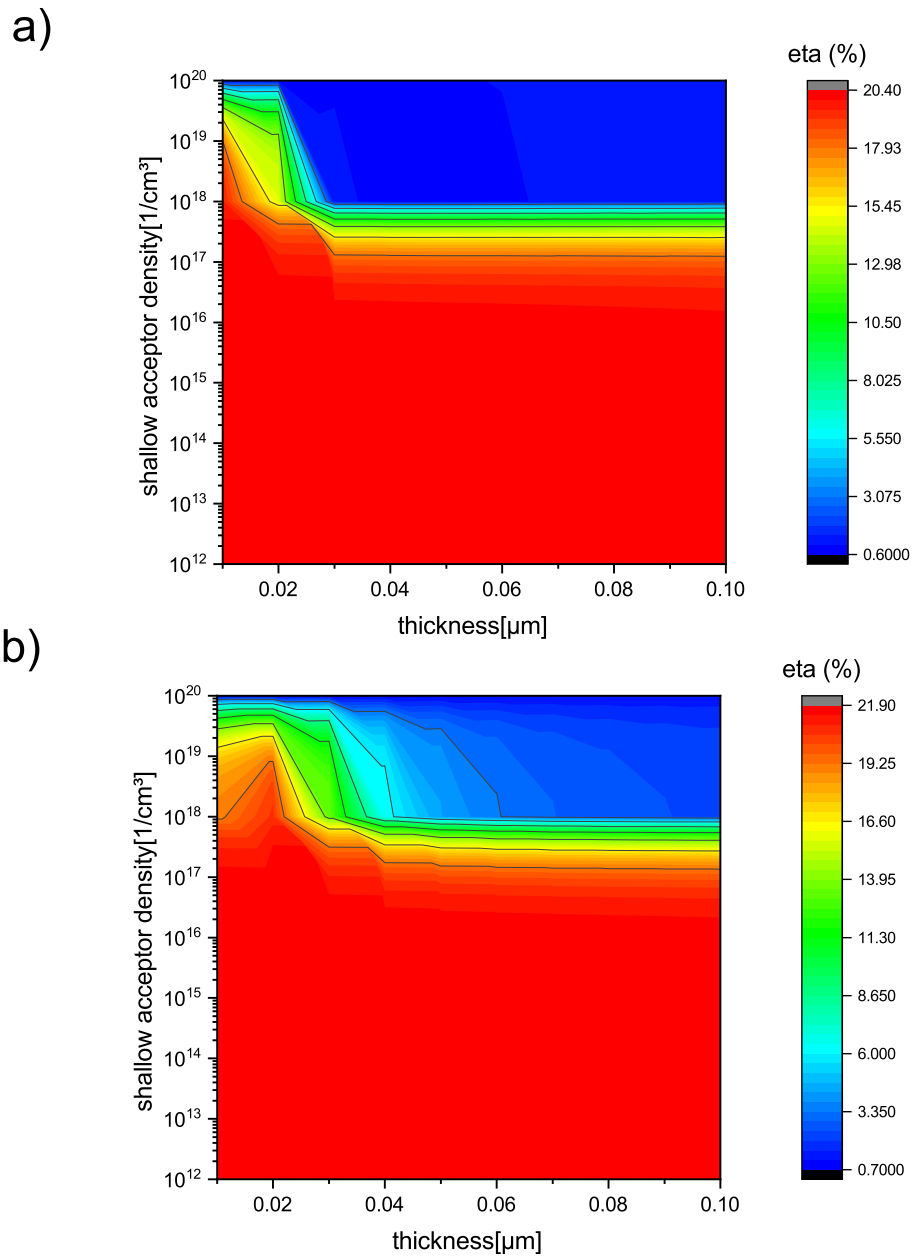


Figure 4.5 Efficiency dependence on OVC thickness and acceptor density for a) double-graded b) single-graded Ga composition.

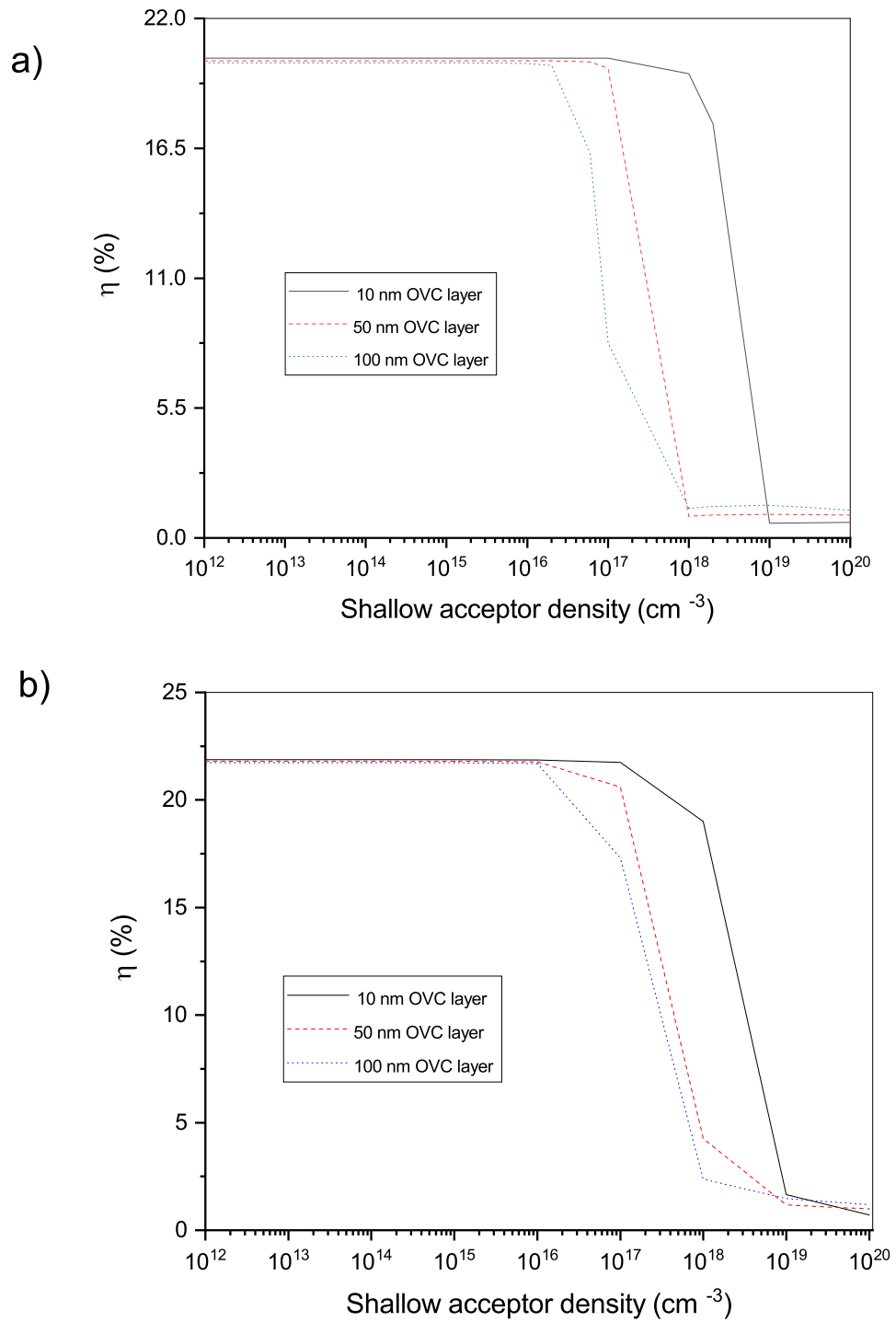


Figure 4.6 Efficiency dependence on acceptor density at various OVC thicknesses for a) double-graded b) single-graded Ga composition.

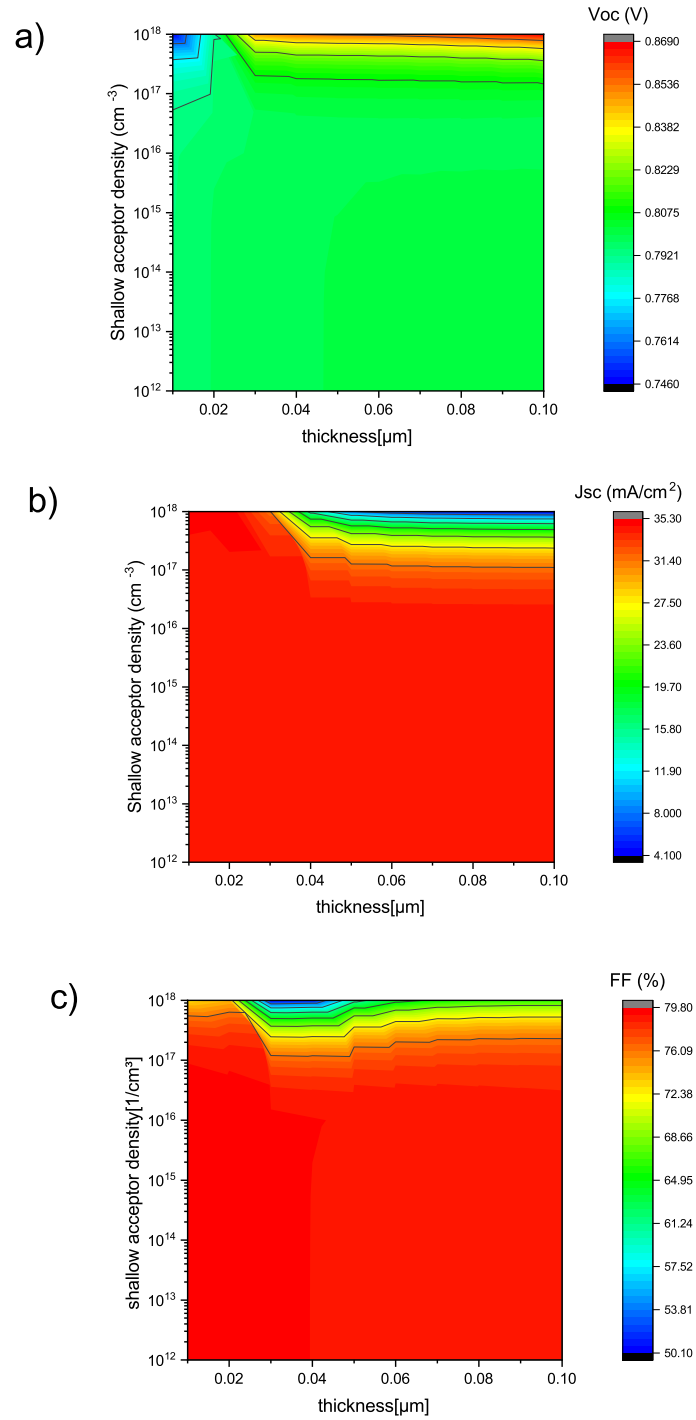


Figure 4.7 a) Open circuit voltage ( $V_{oc}$ ) b) Short circuit current density ( $J_{sc}$ ) c) Fill factor ( $FF$ ) dependence on OVC thickness and acceptor density for single graded Ga composition.

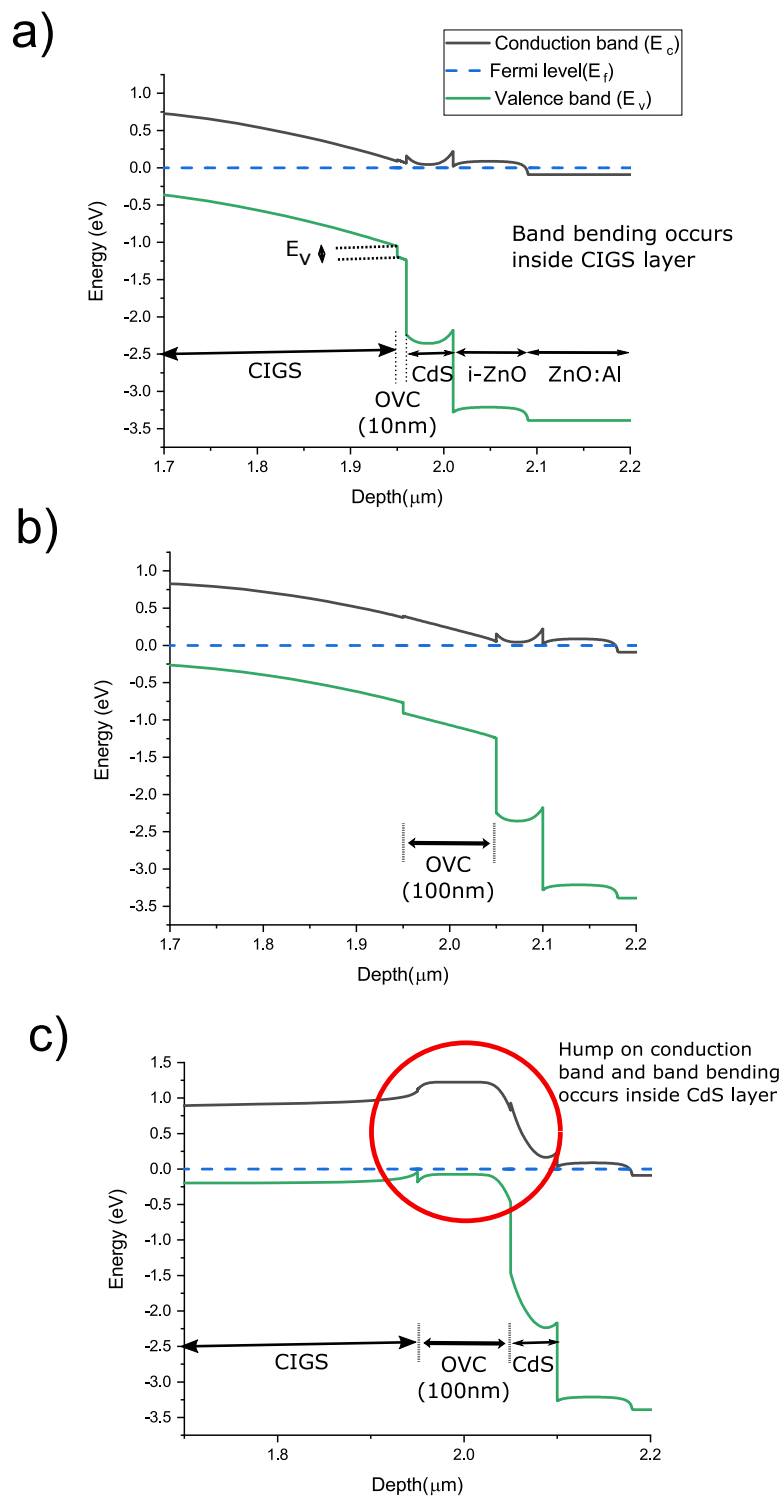


Figure 4.8 Band diagrams at equilibrium (0 V bias voltage) (a) Model A with 10nm OVC layer with doping  $10^{18} \text{ cm}^{-3}$  (b) Model A with 100nm OVC layer with doping  $10^{16} \text{ cm}^{-3}$  (c) Model A with 100nm OVC layer with doping  $10^{18} \text{ cm}^{-3}$ .

#### 4.4 Optimization of The Band-gap and Electron Affinity

Calculations presented in Section 4.2 for midgap donors and shallow acceptors with both single and double graded composition profiles indicated that a 10nm OVC thickness could maintain higher efficiencies ( $\sim 20\%$  for double graded and  $\sim 22\%$  for single graded composition profiles) for shallow acceptors concentration  $\sim 1 \times 10^{16} \text{ cm}^{-3}$ . Therefore optimizing the band gap and electron affinities for both single and double graded composition profiles were carried out for 10 nm thick OVC layer with shallow acceptor density  $N_{A,OVC} = 1 \times 10^{16} \text{ cm}^{-3}$  and mid gap donors density  $N_{t,OVC} = 1 \times 10^{12} \text{ cm}^{-3}$ .

Figure 4.9 (a) and (b) shows efficiency as a function of OVC electron affinity from 4.0 to 4.6 eV and band gap from 1.1 to 1.6 eV for double and single graded Ga compositions. Once again it is evident that the single graded composition has higher efficiency. However, the double graded composition is more stable to variation in  $E_{g,OVC}$  and  $\chi_{OVC}$ . In both cases, the highest efficiencies are maintained over the greatest band gap range for  $\chi_{OVC} = 4.3 - 4.5$  eV. That is due to good conduction band alignment with the CIGS layer which has  $\chi = 4.3$  eV. Efficiency decline can also be observed as  $E_{g,OVC}$  decreases, because  $V_{oc} \propto E_g$ . The direct correlation between  $V_{oc}$ , efficiency, and band gap is evident in Figure 4.10(a), which has the same parameter values as Figure 4.9(b). Figures 4.10 (b) and (c) indicate that  $J_{sc}$  and  $FF$  are not well correlated with efficiency as a function of  $E_{g,OVC}$  and  $\chi_{OVC}$ . Overall, a larger of OVC band gap and affinity in the range of 4.3 - 4.5 eV can provide optimal device performance through increased  $V_{oc}$ . It is important to note, however, that the efficiency is still no greater than the model without OVC layer.

#### 4.5 Band-gap and Defect Density

Figures 4.11 (a) and (b) shows how the efficiency depends on OVC bandgap and mid gap defect concentration for single and double graded compositions. As observed in the previous section, efficiency increases with the increasing OVC bandgap. Figure 4.11 further indicates that efficiency declines as mid-gap defects increases due to a proportional increase in the recombination rate. For example, at  $E_{g,OVC} = 1.3$  eV, efficiency decreases rapidly for  $N_{t,OVC} \geq 10^{16} \text{ cm}^{-3}$  cm.

#### 4.6 Effects of Interface States on EQE

External quantum efficiency for cases with no OVC layer and two OVC thicknesses of 10 nm and 100 nm are shown in Figure 4.12. Recall that the density of interface states,  $N_{it}$ , are different for the cases without OVC (CIGS/CdS interface) and with OVC (OVC/CdS interface), as described in section 3.2. The higher density of defect states for the cases with OVC ( $N_{it} = 10^{12} \text{ cm}^{-2}$ ) compared to the case without OVC ( $N_{it} = 10^{10} \text{ cm}^{-2}$ ) results in slightly lower EQE when no OVC is present. Figure 4.12 also shows that OVC thickness has no effect on EQE for given interface state density. For all calculations in Figure 4.12, the other OVC parameters were  $E_{g,OVC} = 1.3 \text{ eV}$ ,  $\chi_{OVC} = 4.3 \text{ eV}$ ,  $d_{OVC} = 100 \text{ nm}$ ,  $N_{A,OVC} = 10^{16} \text{ cm}^{-3}$ , and  $N_t = 10^{12} \text{ cm}^{-3}$ .

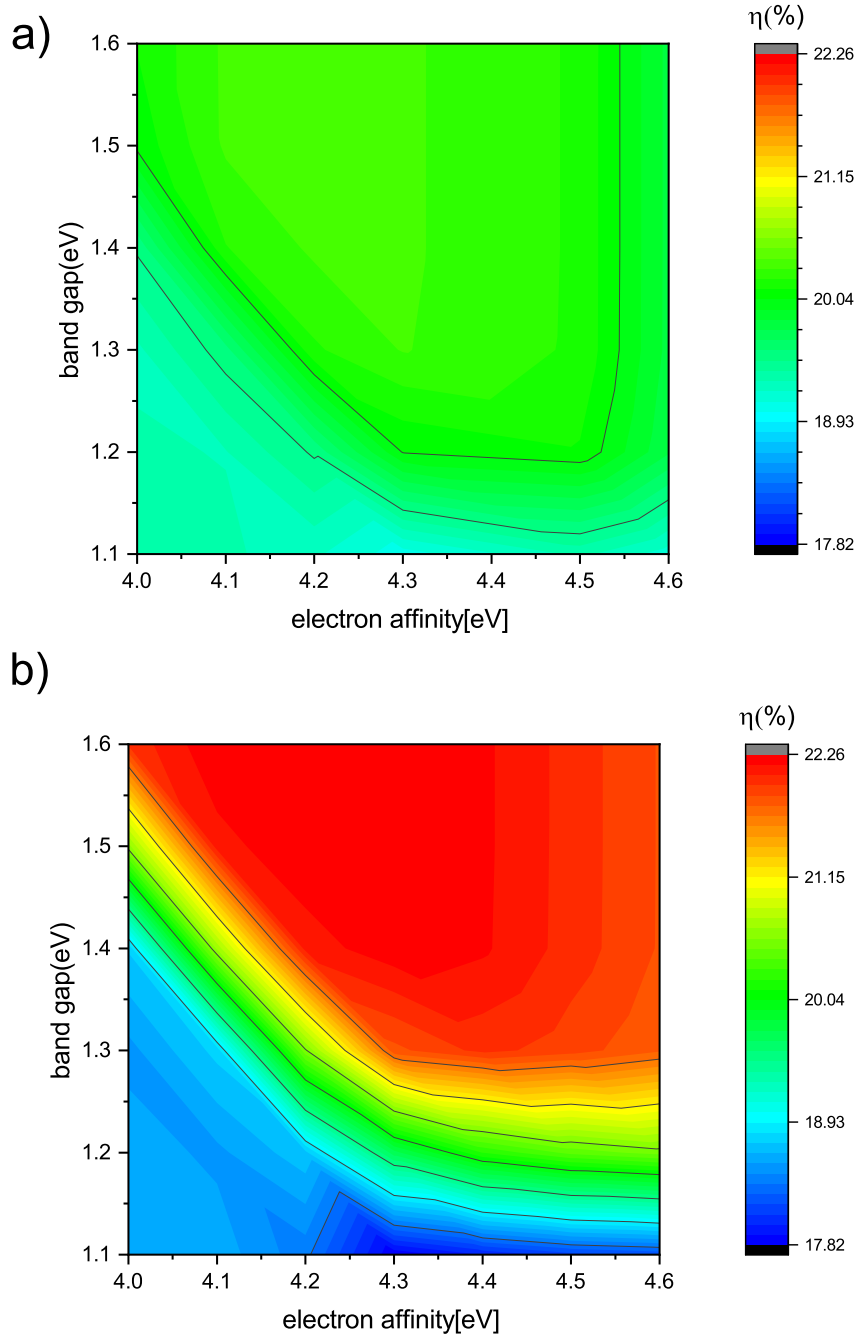


Figure 4.9 Efficiency dependence on OVC band-gap and electron affinity for a) Double graded b) Single graded Ga composition profile for 10nm thick OVC layer Other parameter values are  $N_{A,OVC} = 10^{16} \text{ cm}^{-3}$  and  $N_{t,OVC} = 10^{12} \text{ cm}^{-3}$ .

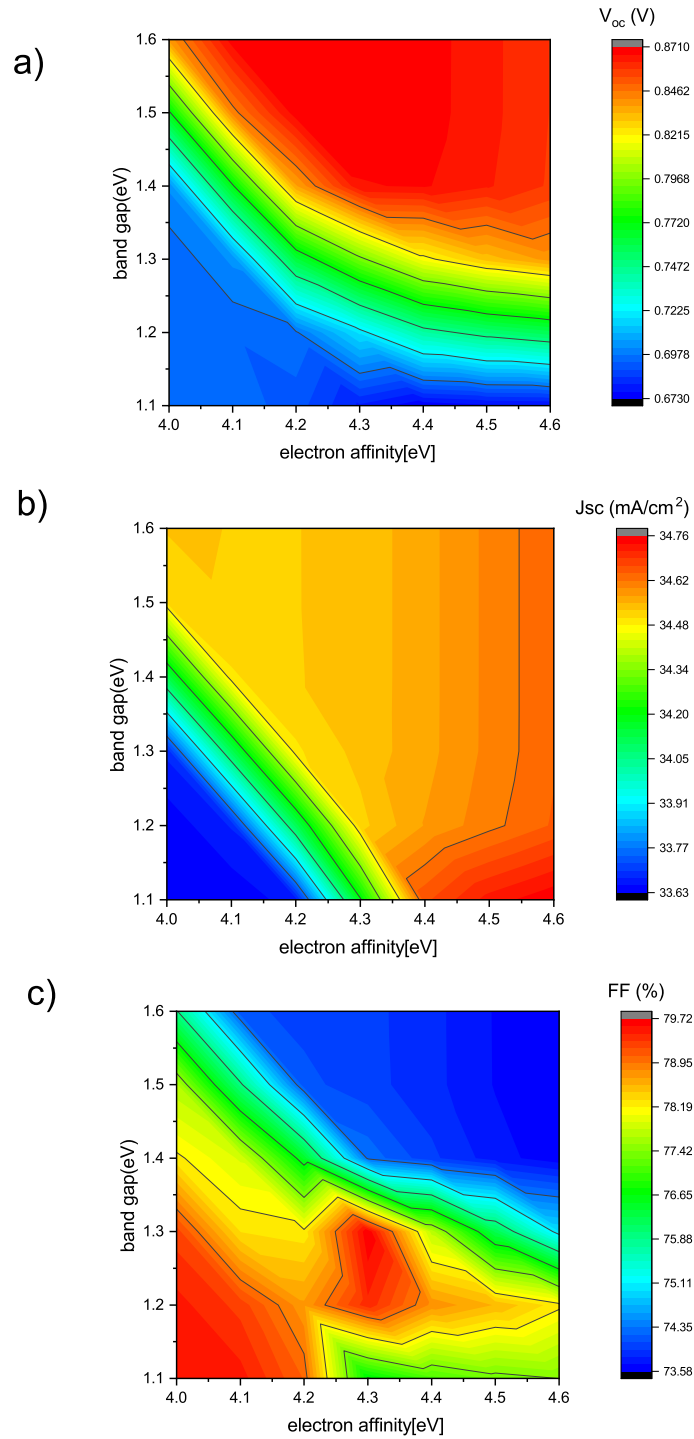


Figure 4.10 a) Open circuit voltage ( $V_{oc}$ ) b) Short circuit current ( $J_{sc}$ ) c) Fill factor ( $FF$ ) dependence on OVC band-gap and electron affinity for single graded Ga concentration for 10nm thick OVC layer.

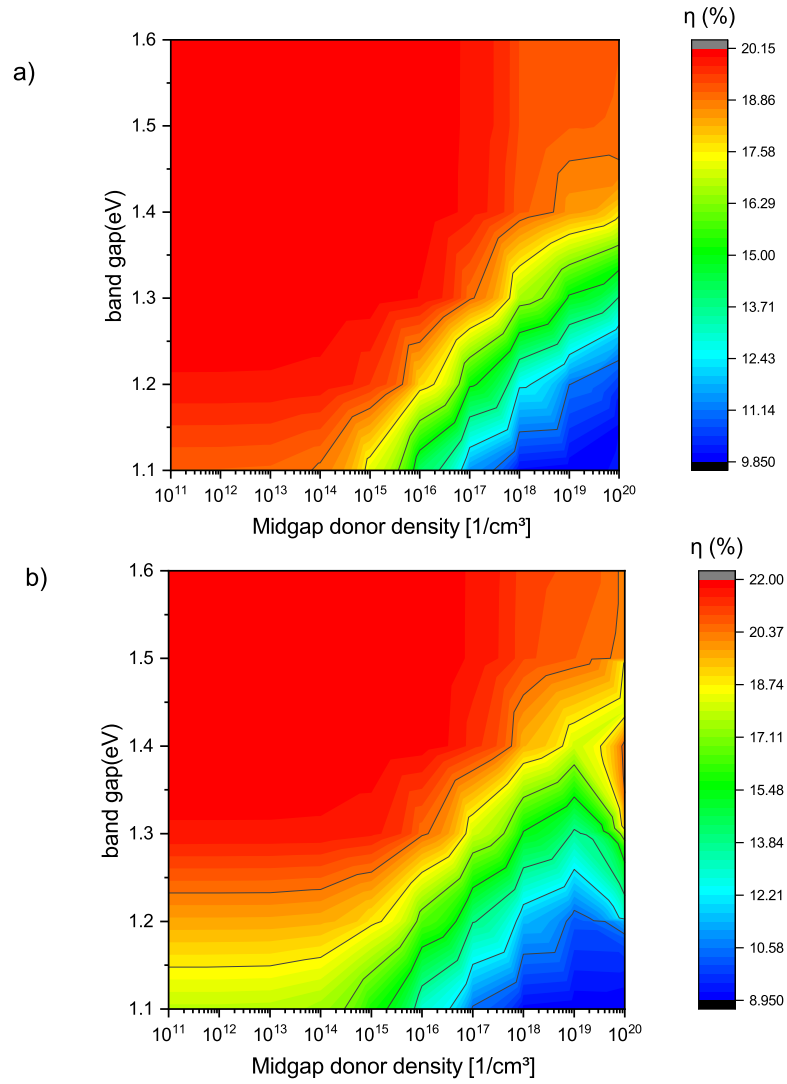


Figure 4.11 Efficiency dependence on OVC band-gap and midgap donor type defects for a) double graded b) single graded Ga composition profile for 100nm thick OVC layer.

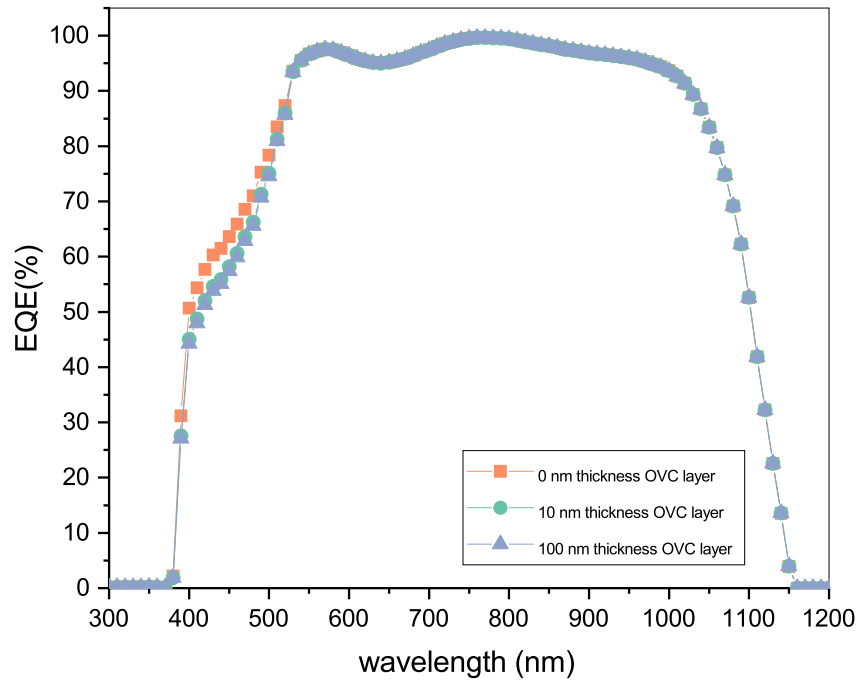


Figure 4.12 External quantum efficiency calculations with 0nm thick OVC layer ( $N_{it} = 10^{10} \text{ cm}^{-2}$ ), 10 nm, and 100 nm thick OVC layer ( $N_{it} = 10^{12} \text{ cm}^{-2}$ ).

## CHAPTER 5 CONCLUSION

In this thesis we have investigated the electronic effects of a Cu-poor layer in the Absorber/Buffer (CIGS/CdS) interface region of CIGS photovoltaic devices. Several previous experimental and theoretical analysis suggested the existence of Cu-poor region in first few 100 nm in to the bulk CIGS from the CIGS/CdS interface. These analysis suggested this Cu-poor region is formed with OVC layer where different stoichiometry of  $\text{CuInGaSe}_2$  exists. Several OVC layer properties are suggested to enhance the overall efficiency of CIGS solar cells. A baseline model without the OVC layer was developed from published models and data. That model (Model A) was extended to include an OVC layer with a range of parameter values based on a literature review. Typical PV device performance metrics were calculated to determine the optimal parameter settings. The following table summarizes our optimized (highest efficiency) results for calculations carried out for Model A with and without OVC layer and with single-graded (SG) and double-graded (DG) CIGS bands gaps.

Table 5.1 Performance metrics of Model A with and without OVC layer

Model	$\eta(\%)$	$V_{oc}$ (mV)	$J_{sc}(\text{mA cm}^{-2})$	FF(%)	$d_{OVC}$ (nm)	$E_{g,OVC}(\text{eV})$	$\chi_{OVC}(\text{eV})$	$N_{A,OVC}(\text{cm}^{-3})$	$N_{t,OVC}(\text{cm}^{-3})$
Baseline, DG (no OVC)	20.5	697	38.3	76.8	NA	NA	NA	NA	NA
Double Graded, with OVC	20.1	694	37.9	76.2	10	1.3-1.6	4.3-4.5	$< 10^{18}$	$< 10^{16}$
Baseline, SG (no OVC)	22.4	830	34.8	74.4	NA	NA	NA	NA	NA
Single Graded, with OVC	22.2	870	34.5	74.0	10	1.3-1.6	4.3-4.6	$< 10^{18}$	$< 10^{16}$

The following are some important observations and results of our analysis of including a OVC layer in a typical CIGS solar cell

- Single graded Ga composition (CIGS bandgap) demonstrated overall higher efficiencies (with maximum  $\eta = 22.2\%$ ) over double graded composition (maximum  $\eta = 20.1\%$ ).
- An OVC band gap of 1.3-1.6 eV and electron affinity of 4.3-4.6 eV provided the highest, stable efficiencies for models that included the OVC layer.
- Mid-gap defect density does not significantly influence the device efficiency for a thin layer of OVC (10 nm). For mid-gap states  $> 10^{16}\text{cm}^{-3}$ , thicker OVC tends to reduce efficiency

through  $V_{oc}$  and  $FF$  loss.

- A thin layer of OVC ( $\sim 10$  nm) could maintain higher density of shallow acceptor defects ( $\sim 10^{18}\text{cm}^{-3}$ ) without effecting the efficiency while a thick OVC layer ( $\sim 100$  nm) could only maintain shallow acceptor defects density of ( $\sim 10^{16}\text{cm}^{-3}$ ), beyond which device efficiency decreased drastically due to poor current collection (low  $J_{sc}$ ).
- Higher acceptor density ( $> 10^{18}\text{cm}^{-3}$ ) shifts the band bending into the CdS layer, causing a hump in the conduction band and which reduces the charge collection and efficiency significantly.
- A valence band offset ( $\Delta E_{v,OVC}$ ) of 0.2 eV was introduced at the OVC/CIGS interface. This offset did not improve the efficiency of the device.
- Although single graded Ga composition resulted higher device efficiency, the double graded composition exhibited more stability against Ga fluctuations (band gap variations).
- The highest device efficiencies were obtained for models without the OVC layer.

Overall, the optimized electronic properties of the OVC layer did not improve device efficiency over the models without the OVC layer. It is important to note that the OVC layer is part of modern CIGS devices because of Cu-poor deposition conditions that are required to avoid often negative effects, such as shunting and high densities of interface states at the heterojunction. This work shows that a single graded band gap with well-passivated interface and no OVC layer could provide higher efficiencies.

## BIBLIOGRAPHY

- [1] Vaughn Nelson and Kenneth Starcher. *Wind energy: renewable energy and the environment*. CRC press, 2018.
- [2] L. El Chaar, L.A. lamont, and N. El Zein. Review of photovoltaic technologies. *Renewable and Sustainable Energy Reviews*, 15(5):2165 – 2175, 2011. ISSN 1364-0321. doi: <https://doi.org/10.1016/j.rser.2011.01.004>. URL <http://www.sciencedirect.com/science/article/pii/S1364032111000050>.
- [3] Taesoo D. Lee and Abasifreke U. Ebong. A review of thin film solar cell technologies and challenges. *Renewable and Sustainable Energy Reviews*, 70:1286 – 1297, 2017. ISSN 1364-0321. doi: <https://doi.org/10.1016/j.rser.2016.12.028>. URL <http://www.sciencedirect.com/science/article/pii/S136403211631070X>.
- [4] T.M. Razykov, C.S. Ferekides, D. Morel, E. Stefanakos, H.S. Ullal, and H.M. Upadhyaya. Solar photovoltaic electricity: Current status and future prospects. *Solar Energy*, 85(8):1580 – 1608, 2011. ISSN 0038-092X. doi: <https://doi.org/10.1016/j.solener.2010.12.002>. URL <http://www.sciencedirect.com/science/article/pii/S0038092X1000366X>. *Progress in Solar Energy* 1.
- [5] Marco Nardone, Yasas Patikirige, Curtis Walkons, Shubhra Bansal, Theresa M Friedlmeier, Kyoung E Kweon, Joel B Varley, and Vincenzo Lordi. Baseline models for three types of cigs cells: Effects of buffer layer and na content. In *2018 IEEE 7th World Conference on Photovoltaic Energy Conversion (WCPEC)(A Joint Conference of 45th IEEE PVSC, 28th PVSEC & 34th EU PVSEC)*, pages 3013–3018. IEEE, 2018.
- [6] Adam Stokes, Mowafak AlJassim, Andrew Norman, David Diercks, and Brian Gorman. Nanoscale insight into the pn junction of alkaliincorporated cu(in,ga)se2 solar cells. *Progress*

- in Photovoltaics: Research and Applications*, 25(9):764772, Apr 2017. ISSN 1099-159X. doi: 10.1002/pip.2883.
- [7] Tetsuya Yamamoto, Koichi Fukuzaki, and Shigemi Kohiki. Influence of incorporation of na on p-type cu<sub>1-x</sub>ga<sub>x</sub>se<sub>2</sub> thin films. *Applied surface science*, 159:345–349, 2000.
- [8] Parag S Vasekar and Neelkanth G Dhere. Effect of sodium addition on cu-deficient cu<sub>1-x</sub>ga<sub>x</sub>se<sub>2</sub> thin film solar cells. *Solar Energy Materials and Solar Cells*, 93(1):69–73, 2009.
- [9] Model for electronic transport in cu<sub>1-x</sub>ga<sub>x</sub>se<sub>2</sub> solar cells. 6. ISSN 1099-159X. doi: 10.1002/(SICI)1099-159X(199811/12)6:6<407::AID-PIP230>3.0.CO;2-U.
- [10] Adam Stokes, Mowafak Al-Jassim, David R. Diercks, Brian Egaas, and Brian Gorman. 3-d point defect density distributions in thin film cu<sub>1-x</sub>ga<sub>x</sub>se<sub>2</sub> measured by atom probe tomography. *Acta Materialia*, Complete(102):3237, 2016. ISSN 1359-6454. doi: 10.1016/j.actamat.2015.09.035.
- [11] Robert Kniese, Michael Powalla, and Uwe Rau. Characterization of the cds/cu<sub>1-x</sub>ga<sub>x</sub>se<sub>2</sub> interface by electron beam induced currents. *Thin Solid Films*, 515(15):61636167, May 2007. ISSN 0040-6090. doi: 10.1016/j.tsf.2006.12.045.
- [12] MT Kibria, A Ahammed, SM Sony, F Hossain, and SU Islam. A review: Comparative studies on different generation solar cells technology. In *Proc. of 5th International Conference on Environmental Aspects of Bangladesh*, 2014.
- [13] Antonio Luque and Steven Hegedus. *Handbook of photovoltaic science and engineering*. John Wiley & Sons 2011.
- [14] Charles E Fritts. On a new form of selenium cell, and some electrical discoveries made by its use. *American Journal of Science*, (156):465–472, 1883.

- [15] Daryl M Chapin, CS Fuller, and GL Pearson. A new silicon p-n junction photocell for converting solar radiation into electrical power. *Journal of Applied Physics*, 25(5):676–677, 1954.
- [16] M. A. Green. Photovoltaics: technology overview. *Energy Policy*, 28(14):989998, 2000. ISSN 0301-4215. doi: [https://doi.org/10.1016/S0301-4215\(00\)00086-0](https://doi.org/10.1016/S0301-4215(00)00086-0).
- [17] Friedrich Kessler and Dominik Rudmann. Technological aspects of flexible cigs solar cells and modules. *Solar Energy*, 77(6):685695, 2004. ISSN 0038-092X. doi: <https://doi.org/10.1016/j.solener.2004.04.010>.
- [18] PC Choubey, A Oudhia, and R Dewangan. A review: Solar cell current scenario and future trends. *Recent Research in Science and Technology*, 4(8), 2012.
- [19] Matthew C Beard, Joseph M Luther, and Arthur J Nozik. The promise and challenge of nanostructured solar cells. *Nature nanotechnology*, 9(12):951, 2014.
- [20] Shruti Sharma, Kamlesh Kumar Jain, and Ashutosh Sharma. Solar cells: in research and applicationsa review. *Materials Sciences and Applications*, 6(12):1145, 2015.
- [21] Jeyakumar Ramanujam and Udai P. Singh. Copper indium gallium selenide based solar cells a review. *Energy Environmental Science*, 10(6):13061319, Jun 2017. ISSN 1754-5706. doi: 10.1039/C7EE00826K.
- [22] Kam Hoe Ong, Ramasamy Agileswari, Biancamaria Maniscalco, Panagiota Arnou, Chakrabarty Chandan Kumar, Jake W. Bowers, and Marayati Bte Marsadek. Review on substrate and molybdenum back contact in cigs thin film solar cell. *International Journal of Photoenergy*, 2018. doi: 10.1155/2018/9106269. URL <https://www.hindawi.com/journals/ijp/2018/9106269/>.
- [23] T. Tinoco, C. Rincn, M. Quintero, and G. Snchez Prez. Phase diagram and optical energy

- gaps for  $\text{CuInGa}_2\text{S}_2$  alloys. *physica status solidi (a)*, 124(2):427–434. doi: 10.1002/pssa.2211240206. URL <https://onlinelibrary.wiley.com/doi/abs/10.1002/pssa.2211240206>.
- [24] Su-Huai Wei and S. B. Zhang. Defect properties of  $\text{CuInSe}_2$  and  $\text{CuGaSe}_2$ . *Journal of Physics and Chemistry of Solids*, 66(11):1994–1999, 2005. ISSN 0022-3697. doi: <https://doi.org/10.1016/j.jpcs.2005.10.003>.
- [25] Shiyong Chen, X. G. Gong, Aron Walsh, and Su-Huai Wei. Electronic structure and stability of quaternary chalcogenide semiconductors derived from cation cross-substitution of  $\text{II-VI}$  and  $\text{I-III-VI}_2$  compounds. *Phys. Rev. B*, 79:165211, Apr 2009. doi: 10.1103/PhysRevB.79.165211. URL <https://link.aps.org/doi/10.1103/PhysRevB.79.165211>.
- [26] Susanne Siebentritt. Alternative buffers for chalcopyrite solar cells. *Solar Energy*, 77(6):767–775, Dec 2004. ISSN 0038-092X. doi: 10.1016/j.solener.2004.06.018.
- [27] Kristijan Brecl, Marko Topi, and Franc Smole. A detailed study of monolithic contacts and electrical losses in a large-area thin-film module. *Progress in Photovoltaics: Research and Applications*, 13(4):297–310. doi: 10.1002/pip.589. URL <https://onlinelibrary.wiley.com/doi/abs/10.1002/pip.589>.
- [28] Takayuki Negami, Takuya Satoh, Yasuhiro Hashimoto, Shiro Nishiwaki, Shin-ichi Shimakawa, and Shigeo Hayashi. Large-area  $\text{CuInGaS}_2$  absorbers prepared by physical vapor deposition. *Solar Energy Materials and Solar Cells*, 67(1):19, Mar 2001. ISSN 0927-0248. doi: 10.1016/S0927-0248(00)00257-9.
- [29] Susanne Siebentritt, Levent G. Bay, David Regesch, Yasuhiro Aida, and Valérie Deprémand. Why do we make  $\text{Cu(In,Ga)Se}_2$  solar cells non-stoichiometric? *Solar Energy Materials and Solar Cells*, 119:1825, Dec 2013. ISSN 0927-0248. doi: 10.1016/j.solmat.2013.04.014.
- [30] Adam Stokes, Brian Gorman, Dave Diercks, Brian Egaas, and Mowafak Al-Jassim. Direct evidence of a  $\text{Cu(In,Ga)}_3\text{Se}_5$  phase in a bulk, high-efficiency  $\text{Cu(In,Ga)Se}_2$  device using

- atom probe tomography. In *2014 IEEE 40th Photovoltaic Specialist Conference (PVSC)*, pages 3335–3337. IEEE, 2014.
- [31] Y Yan, KM Jones, J Abushama, M Young, S Asher, MM Al-Jassim, and R Noufi. Microstructure of surface layers in cu (in, ga) se 2 thin films. *Applied physics letters*, 81(6):1008–1010, 2002.
- [32] MJ Romero, KM Jones, J AbuShama, Y Yan, MM Al-Jassim, and R Noufi. Surface-layer band gap widening in cu (in, ga) se 2 thin films. *Applied physics letters*, 83(23):4731–4733, 2003.
- [33] B Namnuan, V Amornkitbamrung, and S Chatraphorn. Effects of cu (in, ga) 3se5 defect phase layer in cu (in, ga) se2 thin film solar cells. *Journal of Alloys and Compounds*, 2019.
- [34] Takashi Minemoto, Takuya Matsui, Hideyuki Takakura, Yoshihiro Hamakawa, Takayuki Negami, Yasuhiro Hashimoto, Takeshi Uenoyama, and Masatoshi Kitagawa. Theoretical analysis of the effect of conduction band offset of window/cis layers on performance of cis solar cells using device simulation. *Solar Energy Materials and Solar Cells*, 67(1):83 – 88, 2001. ISSN 0927-0248. doi: [https://doi.org/10.1016/S0927-0248\(00\)00266-X](https://doi.org/10.1016/S0927-0248(00)00266-X). URL <http://www.sciencedirect.com/science/article/pii/S092702480000266X>. PVSEC 11 - PART III.
- [35] MM Islam, A Uedono, S Ishibashi, K Tenjinbayashi, T Sakurai, A Yamada, S Ishizuka, K Matsubara, S Niki, and K Akimoto. Impact of cu/iii ratio on the near-surface defects in polycrystalline cugase 2 thin films. *Applied Physics Letters*, 98(11):112105, 2011.
- [36] Raja Mohan and Rini Paulose. Brief review on copper indium gallium diselenide (cigs) solar cells. *Photoenergy and Thin Film Materials*, pages 157–192, 2019.
- [37] Simon M Sze and Kwok K Ng. *Physics of semiconductor devices*. John wiley & sons, 2006.

- [38] Alan Fahrenbruch and RH Bube. Photovoltaic solar energy conversion. *Fundamentals of Solar Cells (Academic Press, New York, 1983)*, 1983.
- [39] H. J. 1. Moller. *Semiconductors for solar cells*. Artech House, Boston, 1993. ISBN 9780890065747;0890065748;.
- [40] Marc Burgelman, Koen Decock, Alex Niemegeers, Johan Verschraegen, and Stefaan Degrave. Scaps manual, 2018.
- [41] RL Anderson. Germanium-gallium arsenide heterojunctions [letter to the editor]. *IBM Journal of Research and Development*, 4(3):283–287, 1960.
- [42] Marc Burgelman, Peter Nollet, and Stefaan Degrave. Modelling polycrystalline semiconductor solar cells. *Thin Solid Films*, 361:527–532, 2000.
- [43] C. Frisk, C. Platzer-Bjrkman, J. Olsson, P. Szaniawski, J. T. Wtjen, V. Fjllstrm, P. Salom, and M. Edoff. Optimizing ga-profiles for highly efficient cu(in, ga)se<sub>2</sub> thin film solar cells in simple and complex defect models. *Journal of Physics D: Applied Physics*, 47(48):485104, 2014. ISSN 0022-3727. doi: 10.1088/0022-3727/47/48/485104.
- [44] Andreas Bauer, Samaneh Sharbati, and Michael Powalla. Systematic survey of suitable buffer and high resistive window layer materials in cuin<sub>1</sub>xgaxse<sub>2</sub> solar cells by numerical simulations. *Solar Energy Materials and Solar Cells*, 165:119127, Jun 2017. ISSN 0927-0248. doi: 10.1016/j.solmat.2016.12.035.
- [45] M.I. Alonso, M. Garriga, C.A. Durante Rincón, E. Hernández, and M. León. Optical functions of chalcopyrite cu<sub>g</sub>axin<sub>1-x</sub>se<sub>2</sub> alloys. *Applied Physics A*, 74(5):659–664, May 2002. ISSN 1432-0630. doi: 10.1007/s003390100931. URL <https://doi.org/10.1007/s003390100931>.
- [46] "high efficiency graded bandgap thin-film polycrystalline cu(in,ga) se<sub>2</sub>-based solar cells". *"Solar Energy Materials and Solar Cells"*, "41-42": "231 – 246", "1996". ISSN

"0927-0248". doi: "https://doi.org/10.1016/0927-0248(95)00145-X". URL "http://www.sciencedirect.com/science/article/pii/092702489500145X",.

- [47] Antonino Parisi, Riccardo Pernice, Vincenzo Rocca, Luciano Curcio, Salvatore Stivala, Alfonso C Cino, Giovanni Cipriani, Vincenzo Di Dio, Giuseppe Ricco Galluzzo, Rosario Miceli, et al. Graded carrier concentration absorber profile for high efficiency cigs solar cells. *International Journal of Photoenergy*, 2015, 2015.
- [48] A Virtuani, E Lotter, M Powalla, U Rau, JH Werner, and M Acciarri. Influence of cu content on electronic transport and shunting behavior of cu(in,ga)se<sub>2</sub> solar cells. *Journal of Applied Physics*, 99(1):014906, 2006.
- [49] Dieter Schmid, Martin Ruckh, F Grunwald, and Hans-Werner Schock. Chalcopyrite/defect chalcopyrite heterojunctions on the basis of cuinse<sub>2</sub>. *Journal of Applied Physics*, 73(6): 2902–2909, 1993.
- [50] Dieter Schmid, Martin Ruckh, and Hans Werner Schock. A comprehensive characterization of the interfaces in mo/cis/cds/zno solar cell structures. *Solar Energy Materials and Solar Cells*, 41:281–294, 1996.
- [51] Takahito Nishimura, Shunsuke Kasashima, Yoshiaki Hirai, Yasuyoshi Kurokawa, and Akira Yamada. Fabrication of cu (in, ga) se<sub>2</sub> solar cells with a single graded band profile. *physica status solidi (b)*, 252(6):1235–1238, 2015.